Near-Field Integration of a SiN Nanobeam and a SiO_{2} Microcavity for Heisenberg-Limited Displacement Sensing

R. Schilling, H. Schütz, A. H. Ghadimi, V. Sudhir, D. J. Wilson, and T. J. Kippenberg

Phys. Rev. Applied **5**, 054019 — Published 26 May 2016

DOI: 10.1103/PhysRevApplied.5.054019

Near-field integration of a SiN nanobeam and a SiO_2 microcavity for Heisenberg-limited displacement sensing

R. Schilling, H. Schütz, A. H. Ghadimi, V. Sudhir, D. J. Wilson, and T. J. Kippenberg
Institute of Condensed Matter Physics, École Polytechnique Fédérale de Lausanne, 1015 Lausanne, Switzerland
(Dated: May 2, 2016)

Placing a nanomechanical object in the evanescent near-field of a high-Q optical microcavity gives access to strong gradient forces and quantum-limited displacement readout, offering an attractive platform for both precision sensing technology and basic quantum optics research. Robustly implementing this platform is challenging, however, as it requires integrating optically smooth surfaces separated by $\lesssim \lambda/10$. Here we describe an exceptionally high-cooperativity, single-chip optonanomechanical transducer based on a high-stress Si_3N_4 nanobeam monolithically integrated into the evanescent near-field of SiO_2 microdisk cavity. Employing a novel vertical integration technique based on planarized sacrificial layers, we realize beam-disk gaps as little as 25 nm while maintaining mechanical $Q \times f > 10^{12}$ Hz and intrinsic optical $Q \sim 10^7$. The combination of low loss, small gap, and parallel-plane geometry results in radio-frequency flexural modes with vacuum optomechanical coupling rates of 100 kHz, single-photon cooperativities in excess of unity, and large zero-point frequency (displacement) noise amplitudes of 10 kHz (fm) $/\sqrt{\text{Hz}}$. In conjunction with the high power handling capacity of SiO_2 and low extraneous substrate noise, the transducer performs particularly well as a sensor, with recent deployment in a 4 K cryostat realizing a displacement imprecision 40 dB below that at the standard quantum limit (SQL) and an imprecision-back-action product $< 5 \cdot \hbar$ (Wilson *et. al.*, **Nature** 524, 325 (2015)). In this report we provide a comprehensive description of device design, fabrication, and characterization, with an emphasis on extending Heisenberg-limited readout to room temperature. Towards this end, we describe a room temperature experiment in which a displacement imprecision 32 dB below that at the SQL and an imprecision-back-action product $< 60 \cdot \hbar$ is achieved. Our results extend the outlook for measurement-based quantum control of nanomechanical oscillators and suggest an alternative platform for functionally-integrated "hybrid" quantum optomechanics.

I. INTRODUCTION

Nanomechanical oscillators [1] are sensitive to feeble forces and exhibit large zero-point fluctuations, making them an attractive platform for both precision sensing technology [2–4] and basic quantum science [5]. Much effort has been devoted to the development of nanomechanical transducers in the electrical domain, including single-electron transistors [6], atomic point contacts [7], and superconducting microwave cavities [8]. Though very successful in recent years [9], these techniques are practically limited by the need for cryogenic operation. A comparatively powerful approach is to parametrically couple a nanomechanical oscillator to an optical cavity. The field of a laser-driven cavity can be quantum-noise-limited at room temperature, and as such represents a practically ideal form of mechanical transducer, with read out enabled by standard interferometric techniques and actuation provided by radiation pressure. Moreover, the finite build-up time of the cavity field allows it to do work on the mechanical element, enabling low-noise optical cooling and amplification [10]. Investigation of these effects has led to two paradigmatic goals in the contemporary field of cavity optomechanics [11]: cooling of a solid-state mechanical oscillator to its ground state and, concomitantly, read-out of its zero-point motion with the minimal disturbance allowed by the Heisenberg uncertainty principle (due to radiation pressure shot noise (RPSN) [12]). The first challenge has been met by several cryogenic optomechanical [13, 14] and electromechanical systems [15] (via resolved-sideband cooling [16]). The latter, corresponding to a measurement at the standard quantum limit (SQL) [17], remains outstanding; however, readout noise far below the zero-point displacement has been reported [18, 19], as well as RPSN dominating the thermal force [20, 21]. Reaching the SQL ultimately requires a 'Heisenberg-limited' displacement sensor for which the product of the read out noise and the total force noise is the minimum allowed by the uncertainty principle. This regime has been approached to within an order of magnitude by several cryogenic systems [15, 18]; it also forms the basis for measurement-based quantum feedback protocols such as ground-state cooling [18, 22] and squeezing [23] of an oscillator.

Efficient cavity optomechanical transduction involves co-localization of optical and mechanical modes with high $Q/(\text{mode volume})$ and high optical power handling capacity. Moreover, it is desirable that the cavity support a mechanism for efficient input/output coupling. A diverse zoo (Fig. 2) of micro- and nanoscale cavity optomechanical systems (COMS) has risen to meet these challenges, ranging from cantilevers [24] and membranes [25] coupled to Fabry-Pérot cavities to mechanically-

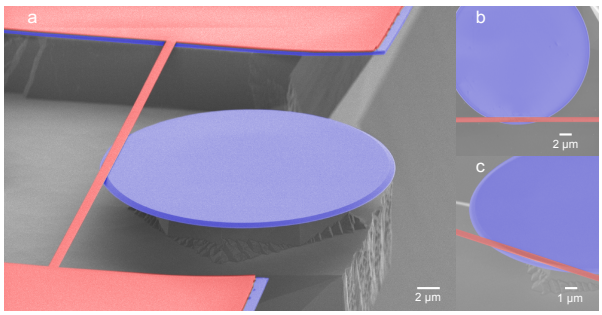

FIG. 1. False-colored scanning electron micrograph of the device: a high-stress Si_3N_4 (red) nanomechanical beam integrated into the evanescent mode volume of a SiO_2 (blue) microdisk. Disk and beam are integrated on a Si (gray) microchip. Subpanel b (c) highlights the lateral (vertical) positioning of the beam.

compliant whispering-gallery-mode (WGM) microcavities [26] and photonic crystals [27]. They generally employ two types of radiation pressure force coupling: traditional scattering-type coupling, in which the cavity field exchanges energy with the mechanical element via momentum transfer, and gradient force coupling [28], in which energy is exchanged via induced-dipole coupling to a field gradient. The net effect is a parametric coupling $G = \partial\omega_c/\partial x$ between the cavity resonance frequency ω_c and the mechanical degree of freedom x, which expresses the force applied per intracavity photon, $\hbar \cdot G$ [11].

A particularly promising platform for optomechanical transduction involves placing a (dielectric) mechanical substrate next to the surface of a WGM microcavity, so that it samples its evanescent field. Since the evanescent decay length is $\sim \lambda/10$, this topology offers the opportunity for strong gradient force coupling to *nanoscale* mechanical devices. It also has the virtue of naturally accomodating optical and mechanical substrates of dissimilar material and geometry, enabling separate optimization of Q/(mode volume). Moreover, WGMs can be input/output coupled with high ideality using tapered optical fibers [29], making them well-suited to interferometric displacement sensing. Recent work has focused on coupling of nano-beams [30], -cantilevers [31], and -membranes [30, 32] to the evancescence of WGM micro-toroids [30], -spheres [32, 33], and -disks [31, 34], with mechanical materials ranging from (ultra low loss) high-stress Si_3N_4 [30] to (ultra low mass) single-layer graphene [32], typically using SiO_2 as the optical material. Gradient force coupling as high as $G \sim 2\pi \cdot 100$ MHz/nm has been achieved [30]. Combined with the high power handling capacity of SiO_2 and low extraneous displacement noise (typically thermo-refractive noise (TRN) in the cavity substrate [35]), optimized systems have achieved room temperature displacement imprecisions as low as $10^{-16}\,\mathrm{m}/\sqrt{\mathrm{Hz}}$, sufficient to in principle resolve the zero-point motion in several cases [30, 35].

Despite these advances, the full potential of evanescent cavity optomechanics has been inhibited by the difficulty of positioning the nanomechanical element within $\lambda/10 \sim 100$ nm of the cavity substrate. Early systems made use of nanopositioning stages and suffered from vibrational stability [30]. Gavartin *et. al.* [34] addressed this challenge by integrating a Si_3N_4 nanobeam and a SiO_2 microdisk on a chip; however, due to fabrication constraints, the beam-disk separation was limited to 250 nm and the optical Q was reduced by a factor of 10.

In this work, we disuss a novel method to monolithically integrate a high-stress Si_3N_4 thin film resonator and a SiO_2 microdisk cavity *within the evanescent near-field*, without deteriorating the intrinsic Q of either element. The critical ingredient is a chemical mechanical polishing (CMP) technique that allows integration of optically flat surfaces with sub-100 nm spacing, separated by a sacrificial film. This procedure is used to carefully isolate Si_3N_4 and SiO_2 layers during wafer processing, allowing high-yield and deterministic fabrication of devices in which a nanobeam is monolithically suspended as little as 25 nm above a SiO_2 microdisk — $\sim 3\times$ smaller than the evanescent decay length of its WGMs — while maintaining mechanical and optical mode qualities in excess of 10^5 and 10^6, respectively. The process is compatible with e-beam lithography, thus we are able to locally pattern the beam with sub-10 nm imprecision (opening the door to stress engineering [36]) and laterally position it with sub-100 nm imprecision across a full 4" Si wafer.

A typical device is shown in Fig. 1, corresponding to a $60 \times 1 \times 0.06\,\mu\mathrm{m}^3$ beam positioned 25 nm above a 0.65-μm-thick, 25-μm-diameter microdisk. By carefully varying the dimensions of the beam, the disk, and their lateral offset with respect to this nominal geometry, we achieve optomechanical coupling rates (G) in excess of $2\pi \cdot 1$ GHz/nm while maintaining cavity decay rates (κ) as low as $2\pi \cdot 100$ MHz and radio frequency ($\Omega_m = 2\pi \cdot (1-10)$ MHz) flexural beam modes with damping rates (Γ_m) as low as 10 Hz. In conjunction with the small mass ($m \sim 10$ pg) and large zero-point displacement ($x_{zp} \equiv \sqrt{\hbar/2m\Omega_m} \sim 10$ fm) of the beam modes, the combined low-loss, small gap and parralel-plane geometry result in a vacuum optomechanical coupling rates ($g_0 \equiv G \cdot x_{zp}$) as high as $2\pi \cdot 100$ kHz and room temperature single-photon cooperativies as high as $\mathcal{C}_0 \equiv 4g_0^2/\kappa\Gamma_m = 2$. The latter is notably a factor of 10^5 times larger than in [34] and on par with the state-of-the-art for both room temperature and cryogenic COMS (Fig. 2).

In conjunction with high $\mathcal{C}_0$, several features of the system make it well-suited for quantum-limited operation. First, SiO_2 microcavities with the reported dimensions and internal loss readily support intracavity photon numbers of $n_c \sim 10^6$. This enables quantum cooperativities ($C_0 n_c/n_{th}$) approaching unity — a basic requirement for performing a Heisenberg-limited displacement measurement — for a room temperature thermal occupation of $n_{th} \approx k_B T/\hbar\Omega_m \sim 10^6$, corresponding to $\Omega_m \sim 2\pi \cdot 5$ MHz. Another striking feature is the exceptionally large magnitude of the cavity frequency noise produced by zero-point motion of the mechanical oscillator, $S_\omega^{zp}(\Omega_m) \equiv 4g_0^2/\Gamma_m \sim 10\,\mathrm{kHz}/\sqrt{\mathrm{Hz}}$. This magnitude is many orders of magnitude larger than typical extraneous sources of noise due to laser frequency fluctuations or TRN [35]. Taking advantage of these strengths, recent deployment of the device in a 4 K Helium crystat enabled interferometric measurements with a read-out noise 43 dB below $S_\omega^{zp}(\Omega_m)$ (corresponding to an imprecision 40 dB below that necessary to reach the SQL) and with an imprecision-back-action product of $5 \cdot \hbar$, allowing active feedback cooling to near the motional ground

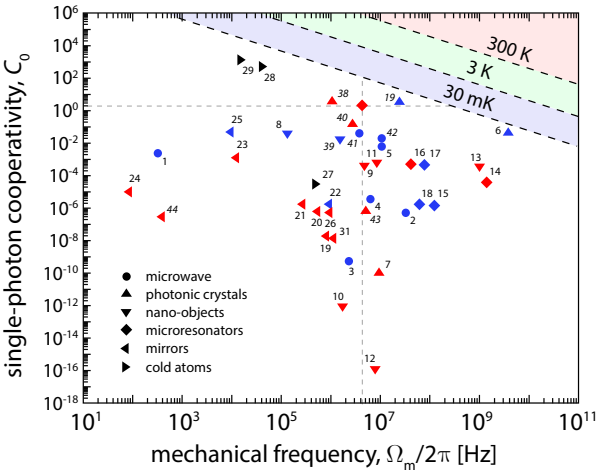

FIG. 2. Survey of single-photon cooperativity $\mathcal{C}_0 = 4g_0^2/\kappa\Gamma_m$ for various cavity optomechanical systems [19, 37–43], adapted with permission from [11]. Non-italicized references are cited in [11]. Blue and red points correspond to cryogenic (typically $T < 10$ K) and room temperature experiments, respectively. Diagonal lines indicate the condition for $\mathcal{C}_0 = n_{th} \approx k_B T/\hbar\Omega_m$, for various T. The reported result is highlighted with crosshairs.

state [18]. Below, we demonstrate a measurement with an imprecision 32 dB below that at the SQL and an imprecision-back-action product of $60 \cdot \hbar$, using a moderate input power of 10 μW. Remarkably, the imprecision due to microdisk TRN [35] can be 20 dB lower.

In the following sections we carefully detail the design, fabrication, and characterization of the device, and provide a demonstration of low noise displacement measurement. Sec. II gives an overview of nanobeam and microdisk resonators and describes a numerical model used to predict their gradient-force optomechanical coupling. Notably, we find that G can be improved by an order of magnitude by carefully positioning the beam above the disk. Sec. III describes the fabrication method, particularly the use of planarized (by CMP) sacrificial layers and e-beam lithography, which enable precise engineering of the vertical and horizontal beam-disk separation, respectively. Sec. IV describes characterization of the device using thermomechanical noise measurements and the optical spring effect. In Sec. V, we discuss an experiment in which the microdisk is embedded into fiber-based homodyne interferometer, enabling displacement read-out with an imprecision 35 dB below $S_\omega^{\rm zp}(\Omega_{\rm m})$ for the fundamental beam mode. Finally, in Sec. VI, we remark on the feasibility of Heisenberg-limited position measurements and alternative applications which taking advantage of heterogeneous integration method.

II. DEVICE DESIGN

A. Nanomechanical beam

The mechanical resonator we study is a doubly-clamped beam released from a high-stress Si_3N_4 thin film [44]. Stressed "nanobeams" are attractive for their string-like flexural modes, which possess exceptionally high Q/m ratios [45]. Beams with of the dimensions studied — $\{\text{length}\,(l), \text{width}\,(w), \text{thickness}\,(t)\} \sim \{100, 1, 0.1\}$ μm — possess effective masses $m \sim 10$ pg, fundamental frequencies $\Omega_{\rm m} \sim 2\pi \cdot 10$ MHz and room temperature quality factors $Q_{\rm m} > 10^5$ [44]. Significantly, $Q_{\rm m}$ is well in excess of the "universal" value of $10^3 - 10^4$ observed for bulk amorphous glass resonators at temperatures above $T \gtrsim 1$ K [46]. It is also higher than for typical unstressed, single-crystal nanobeams due to surface loss [47]. This exceptional behavior is known to derive from a combination of large impedance mismatch from the anchoring body [48] (suppressing extrinsic loss) and stress-related "dilution" of intrinsic loss [47, 49–51]. From the standpoint of quantum-limited measurement, an important consequence of their high Q/m is that high-stress nanobeams exhibit large zero-point fluctuations. Expressed as a single-sided spectral density evaluated at the mechanical frequency, the above parameters correspond to a peak zero-point displacement noise density of $S_x^{\rm zp}(\Omega_{\rm m}) = 2\hbar Q_{\rm m}/m\Omega_m^2 \sim 10$ fm/$\sqrt{\rm Hz}$. This value occurs in a radio frequency window, 1-10 MHz, where low noise electronics and laser sources are readily available; as such, nanobeams were the first solid-state mechanical resonators to be read out electrically [52] and optically [35] with an imprecision lower than $S_x^{\rm zp}(\Omega_{\rm m})$.

Measurements of $Q_{\rm m}$ for a typical disk-integrated beam with dimensions $\{l, w, t\} = \{60, 0.6, 0.06\}$ μm are shown in Fig. 3. Despite the complexity of the fabrication procedure (Sec. III), flexural modes exhibit $Q_{\rm m} \cdot \Omega_{\rm m}/2\pi$ as high as $4 \cdot 10^{12}$ Hz, on par with the state-of-the-art for high-stress Si_3N_4 nanobeams of similar dimensions [47, 53]. The near-linear eigenfrequency spectrum, $\Omega_{\rm m}^{(n)} \approx 2\pi n \cdot 4.3$ MHz, is consistent with a tensile stress of $\mathcal{T} \approx (\rho l \Omega_m^{(0)}/\pi)^2 \approx 0.8$ MPa assuming a density

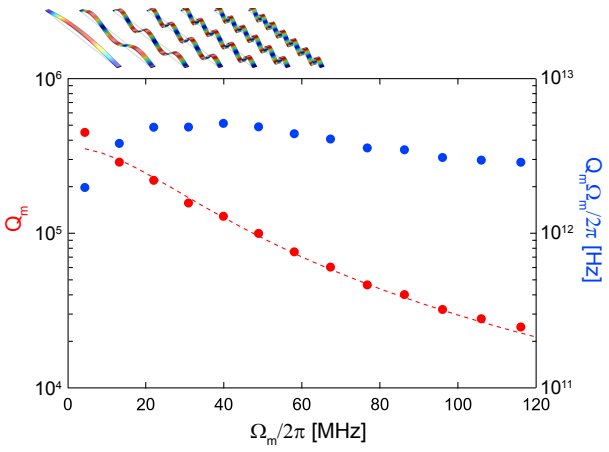

FIG. 3. Q-factor (red) and $Q \times$ frequency product (blue) of the first eleven, odd-ordered, out-of-plane flexural modes of a nanobeam with dimensions $\{l, w, t\} = \{60, 0.6, 0.05\}$ μm. Solid red curve is a fit to the Q-dilution model in [47], implying a limiting contribution from surface-related intrinsic loss.

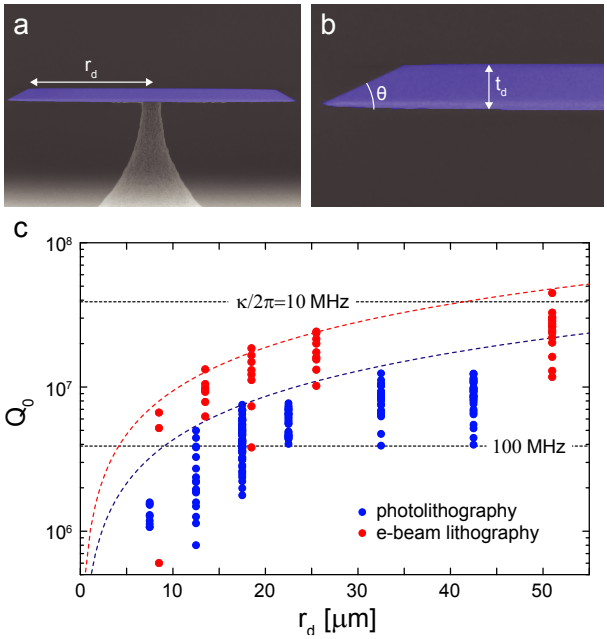

FIG. 4. (a,b) SEM of a wedged microdisk; blue and gray indicate SiO_2 and Si, respectively. (c) WGM quality factor Q_o as a function of disk radius r_d for standalone SiO_2 microdisks of thickness $t_d \approx 700$ nm. TE and TM modes are not distinguished. Blue (red) points correspond to disks prepared with photolithoghraphy (e-beam lithography), which produce wedge angles of $\theta \approx 30(11)^\circ$. Horizontal lines represent constant cavity linewidth, $\kappa = 2\pi c/(\lambda Q_o)$, with $\lambda = 780$ nm. Blue (red) dashed line is a guide-to-the-eye for $Q \propto r_d$, corresponding to a fixed finesse of $\mathcal{F} = 0.6\ (1.2) \cdot 10^5$.

of $\rho = 2700$ kg/m^3 [44]. The mechanical-Q spectrum, $Q_m^{(n)} \approx 3.6 \cdot 10^5/(1 + 0.023 \cdot n^2)$, is consistent with the intrinsic loss model of [47, 50]. The dashed line in Fig. 3 is a fit to this model: $Q_m^{(n)} = Q_{int}/(\lambda + n^2\pi^2\lambda^2)$, where $\lambda^2 = Et^2/(12\mathcal{T}l^2)$, E is the elastic modulus of the film, and Q_{int} is the intrinsic quality factor of the film when unstressed. The inferred value of $Q_{int} \approx 6700$ (using $E = 200$ GPa), is roughly an order of magnitude lower than that for bulk Si_3N_4. Interpreted as surface loss, however, the inferred coefficient of $Q_{int}/t \approx 1.1 \cdot 10^5$ μm^{-1} is within a factor of two of the typical value for LPCVD SiN thin films [47]. Operating in a ^{3}He cryostat at 4 K, we have recently observed $Q_{int} > 10^4$ [18].

In addition to its favorable mechanical properties when stressed, Si_3N_4 is an attractive optical material. It has a relatively large index of refraction, $n \approx 2$, and, owing to its ~ 3 eV bandgap, respectably low optical absorption at near infrared wavelengths, characterized by an imaginary index of $n_{im} \sim 10^{-5} - 10^{-6}$ [54].

B. Optical microdisk

The optical resonator we employ is a SiO_2 microdisk supporting WGMs along its periphery. SiO_2 microdisks possess several advantages for evanescent sensing. The first advantage is that SiO_2 exhibits a wide transparency window and a large power handling capacity, enabling large intracavity photon numbers (n_c). The practically achievable n_c is typically limited by Kerr and Raman nonlinearity. At visible and telecommuncation wavelengths, other effects such as multi-photon absorption do not play a significant role in SiO_2, in contrast to Si and other semiconductors. A second advantage is that standard lithographic techniques, in conjunction with wet-etching, can produce SiO_2 microdisks with exceptionally high Q (recently exceeding 10^7 in the telecommunication band [55, 56]). This feature is related to the wedged rim of the disk, which supports WGMs that are spatially isolated from the surface, and thereby from surface scattering/absorption loss. A third advantage is that microdisk WGMs can be evanescently coupled to tapered optical fibers with high ideality [29]. This feature is critical for sensing applications, in which optical loss produces elevated shot-noise imprecision [26].

Microdisk resonators were in this case studied at $\lambda \approx 700 - 800$ nm (outside of the telecommunications window), to allow for smaller optical mode volumes. As discussed in Sec. II C, reducing the disk radius (r_d) and thickness ($t_d \sim \lambda/n$) results in smaller mode volumes with fractionally larger evanescent components, thereby increasing the optomechanical coupling strength. Fig. 4 shows measurements (see Sec. IV A for details) of optical Q versus disk radius (r_d) for microdisk samples of thickness $t_d = 0.7$ μm . Two sets of devices are considered. The first set was prepared with photolithography, the second with electron-beam lithography. The sets differ by their corresponding wedge angle, which is 30 (11) degrees for wet (e-beam) lithography. For both disk preparation methods, intrinsic $Q > 10^6$ was measured for radii as low as 10 μm, corresponding to loss rates of $\kappa \sim 2\pi \cdot 100$ MHz. For shallower wedge angles, Q as high as $4 \cdot 10^7$ ($\kappa \sim 2\pi \cdot 10$MHz) was obtained — notably similar to those measured at telecommunications wavelengths, where scattering losses are significantly lower [56, 57]. Numerical simulations [58] reveal that radiation contributes negligibly to the measured loss. Dotted blue (red) lines in Fig. 4 are guide-to-the-eye models for $Q \propto r_d$, consistent with loss due to surface absorption/scattering [59], and corresponding to a fixed finesse of $\mathcal{F} \equiv \Delta\omega_{FSR}/\kappa \approx c/(r_d\kappa) = 0.6\ (1.2) \cdot 10^5$. As discussed in Sec. IV D, the intrinsic microdisk Q is ultimately reduced by loss introduced by the nanobeam, for beam-disk separations of less than 100 nm.

C. Evanescent optomechanical coupling

Optomechanical coupling is achieved by placing the nanobeam near the surface of the microdisk, so that its mid-section occupies the evanescent volume of one of the microdisk WGMs. When the WGM is excited, the beam experiences a gradient force, F_{opt}. The magnitude of this force, and likewise the optomechanical coupling factor $G = \partial\omega_c/\partial x$, can be derived by computing the work done on the WGM, $-\delta U_{cav}$, by a small displacement of the beam, δx: that is, $F_{opt} = -\partial U_{cav}/\partial x \approx -GU_{cav}/\omega_c$, where U_{cav} is the potential energy stored in the cavity field [28, 60]. To first order, it can be shown that [30]

$$G \approx \frac{\omega_c^{(0)}}{2}\frac{\partial}{\partial x}\left(\frac{\int_{beam}(\epsilon(\vec{r})-1)|\vec{E}^{(0)}(\vec{r})|^2 d^3r}{\int_{disk}\epsilon(\vec{r})|\vec{E}^{(0)}(\vec{r})|^2 d^3r}\right) \quad (1a)$$

$$\approx \frac{\omega_c^{(0)}}{2}\frac{\partial}{\partial x}\left(\frac{n_{SiN}^2-1}{n_{SiO_2}}\frac{|E_{max}^{(0,beam)}|^2}{|E_{max}^{(0,disk)}|^2}\frac{V_{beam}}{V_{disk}}\right) \quad (1b)$$

where $\epsilon(\vec{r})$ is the local relative permittivity, $\vec{E}^{(0)}(\vec{r})$ is the unperturbed cavity field amplitude, and

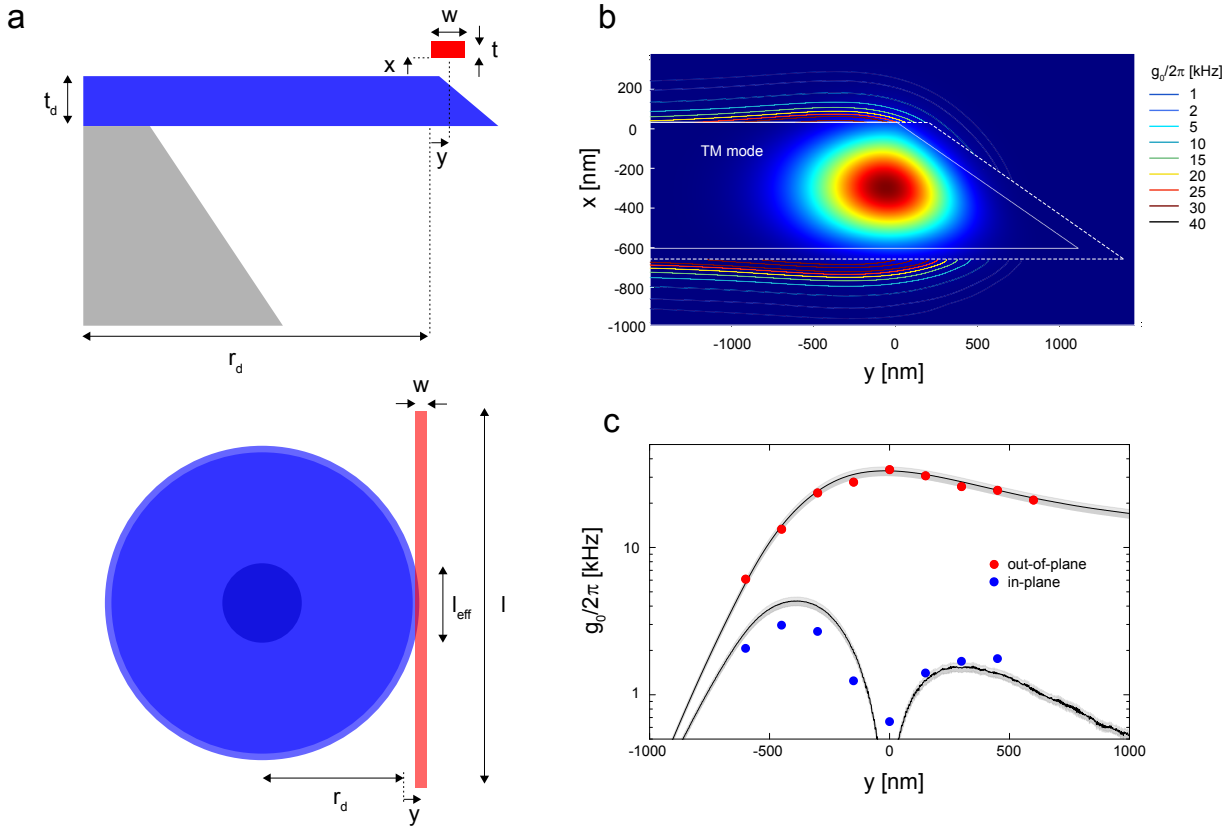

FIG. 5. (a) Geometry of the nanobeam-microdisk system: x, y represent the vertical (out-of-plane) and lateral (in-plane) position of the beam, respectively, with respect to the inner rim of the disk (thickness t_d, radius r_d). (b) Simulated optomechanical coupling versus beam position for the device shown in Fig. 1. The intensity profile of a TM-like WGM (computed using finite element analysis) is shown in the background. Solid and dashed white lines denote the disk surface and the boundary within which the beam touches the disk surface, for the coordinate system defined in (a). Contours indicate lines of constant g_0 for the 4.3 MHz fundamental out-of-plane mode. (c) Measured and simulated g_0 versus y for the beam shown in Fig. 1. Black and blue data are for fundamental out-of-plane and in-plane vibrational modes, respectively (for details, see Sec. IV D). Black lines correspond to numerical solutions to Eq. 1 with a vertical offset of $x = 25$ nm. Gray shading shows the solution space for x =20 to 30 nm.

$\int_{\mathrm{beam(disk)}}$ indicates an integral over the volume occupied by the beam (disk). The simplified expression in Eq. 1b replaces ϵ with an index of refraction n and parameterizes each integral in terms of the intensity-weighted volume of the beam (disk), $V_{\mathrm{beam(disk)}} \equiv \int_{\mathrm{beam(disk)}} |E_0|^2 d^3r / |E_{\mathrm{max}}^{(0,\mathrm{beam(disk)})}|^2$, where $E_{\mathrm{max}}^{(0,\mathrm{beam(disk)})}$ is the maximum of the unperturbed field within the beam (disk).

To gain physical insight into Eq. 1, we consider the configuration shown in Fig. 5. Here the beam is placed above the disk, so that it samples the vertical evanescence of a WGM. For simplicity, the transverse dimensions of the beam are assumed to be much smaller than that of the evanescent field; that is, $w \ll \sqrt{A_{\mathrm{WGM}}}$ and $w \ll x_{\mathrm{ev}}$, where A_{WGM} is the effective cross-sectional area of the WGM and x_{ev} is the exponential decay length of the evanescent field. In this case V_{beam} can be approximated as twl_{eff}, where $l_{\mathrm{eff}} < l$ is the intensity-weighted "sampling length" of the beam. Likewise V_{disk} can be parameterized as $V_{\mathrm{disk}} \approx 2\pi r_d A_{\mathrm{WGM}}$, where r_d is the physical disk radius. Assuming the form $|E_{\mathrm{max}}^{(0,\mathrm{beam})}|/|E_{\mathrm{max}}^{(0,\mathrm{disk})}| = \xi e^{-\frac{x+t/2}{x_{\mathrm{ev}}}}$, neglecting the weak position dependence of V_{beam}, and assuming the effective mass of a point probe, $m = \rho twl/2$, the vacuum optomechanical coupling rate can be approximated as

$$g_0 \approx \frac{1}{2}\frac{\omega_c^{(0)}}{x_{\mathrm{ev}}}\frac{n_{\mathrm{SiN}}^2 - 1}{n_{\mathrm{SiO_2}}}\frac{twl_{\mathrm{eff}}}{2\pi r_d A_{\mathrm{WGM}}}\xi^2 e^{-\frac{x+t/2}{x_{\mathrm{ev}}}} \cdot \sqrt{\frac{\hbar}{\rho twl\Omega_m}} \quad (2)$$

where ρ is the mass density of the beam. In practice x_{ev}, A_{WGM}, and ξ must be determined numerically for a wedged microdisk. An estimate can be made, however, by assuming the mode shape of a microtoroid WGM with a minor radius of $t_d/2$ [30]. In this case, using $n_{\mathrm{SiO_2}} \approx 1.4$, one has $x_{\mathrm{ev}} \approx \lambda/(2\pi\sqrt{n_{\mathrm{SiO_2}}^2 - 1}) \approx \lambda/12$, $A_{\mathrm{WGM}} \approx 0.15 r_d^{7/12} t_d^{1/4} \lambda^{7/6}$ and $\xi \approx 1.1(\lambda/r_d)^{1/3}$ [61]. Using these formulas, the device geometry in Fig. 1 ($\{t, w, l\} = \{0.06, 0.4, 60\}$ μm, $x = 25$ nm, $r_d = 14.2$ μm, $t = 0.65$ μm) and assuming $\lambda = 780$ nm, $n_{\mathrm{SiN}} = 2.0$, $\rho = 2700$ kg/m^3, $\Omega_m = 2\pi \cdot 4.3$ MHz, and $l_{\mathrm{eff}} = 10$ μm (see Sec. IV F), Eq. 2 predicts that $G \approx 2\pi \cdot 1.0$ GHz/nm, $x_{\mathrm{zp}} \approx 33$ fm, and $g_0 = 2\pi \cdot 33$ kHz. As shown in Fig. 5d, This estimate agrees well with numerically and experimentally determined values. Notably, Eq. 2 implies that to achieve large g_0, it is necessary to reduce the vertical gap to $x < x_{\mathrm{ev}} \approx 100$ nm, and to maximize l_{eff} by laterally positioning the beam *above* the disk.

A numerical model for $g_0(x, y)$ is shown in Fig. 5b. Intrinsic WGM mode shapes, $\vec{E}^{0)}(\vec{r})$, were computed us-

ing an axially-symmetric finite element model (COMSOL FEM axial symmetric package [58]). The energy stored in the WGM, $U_{\rm cav}^{(0)} \approx \frac{1}{2}\int_{\rm disk}\epsilon(\vec{r})|\vec{E}^{(0)}(\vec{r})|^2 d^3r$, and the energy shift due to the beam, $\Delta U_{\rm cav}(x,y) \approx \frac{1}{4}\int_{\rm beam}(\epsilon(\vec{r})-1)|\vec{E}^{(0)}(\vec{r})|^2 d^3r$, were computed by numerical integration in Matlab. Differentiating the 2D energy landscape gives $G(x,y) = \omega_{\rm c}\frac{\partial}{\partial x}(\Delta U_{\rm cav}(x,y)/U_{\rm cav}^{(0)})$ for out-plane-motion. Fig. 5b shows $g_0(x,y) = G(x,y)\cdot x_{\rm zp}$ for a beam and disk with the dimensions given above, for a TM-like WGM mode. Contours indicate that the optimal position of the beam is above and inside the inner rim of the disk, and that the magnitude of g_0 scales exponentially with vertical displacement from the disk surface, with a decay length of ~ 100 nm. A horizontal cut through the contours for $x = 25$ nm is shown in Fig. 5c. Upper and lower curves show models for fundamental in-plane (IP) and out-of-plane (OP) flexural modes. Significantly, maximizing $g_0^{(\rm OP)}$ also minimizes $g_0^{(\rm IP)}$; this opens a wide spectral window, $\Delta\Omega \sim \Omega_{\rm m}$, for measurement of the out-of-plane mode. Experimental measurements (see Sec. IV B) of $g_0(25\text{ nm}, y)$ are also shown in Fig. 5c . The model agrees well with experiment assuming a vertical offset of 25 ± 5 nm.

III. DEVICE FABRICATION

The fabrication process is outlined in Fig. 6. Four key elements of the process, detailed in the following subsections, are: (A) fabrication of the SiO_2 microdisk, (B) formation of a planarized sacrificial layer, (C) fabrication of the Si_3N_4 nanobeam, and (D) release of the sacrificial layer. Of particular importance is the sacrificial layer, which allows the mechanical (Si_3N_4) and optical (SiO_2) elements to be designed independently while maintaining the high optical quality and achieving a vertical beam-disk separation of less than 100 nm. Also important is the use of e-beam lithography to pattern the Si_3N_4, as this enables fine tuning of the lateral beam position.

A. Microdisk fabrication

The process begins with an undoped, float-zone (FZ) Si wafer, on which a 750 nm film of SiO_2 is grown by dry oxidation. Three structures are patterned into the SiO_2 film: the microdisk, rectangular pads that later serve as a platform for the nanobeam and a reference plane for CMP polishing, and markers that are later used for e-beam alignment. As illustrated in Fig. 7, the SiO_2 pattern is processed in two stages. In the first stage all structures are defined. In the second stage the microdisk is etched preferentially, recessing it from the pads and defining the vertical gap between disk and the beam.

Details of the SiO_2 patterning process are as follows: The first mask, containing all structures, is exposed in 1.1 μm of Microchemicals AZ 1512 photoresist using a Karl Süss MA 150 mask aligner and a broadband Hg lamp. A subsequent reflow step is used to smooth the pattern boundaries and minimize standing wave patterns. Afterwards, the pattern is transfered to SiO_2 by etching in a room-temperature bath of BHF. The photoresist is then stripped and a second mask is applied. The second mask covers all structures on the wafer except for the microdisk, leaving it exposed for etching (Fig. 7a). The microdisk is preferentially etched in BHF

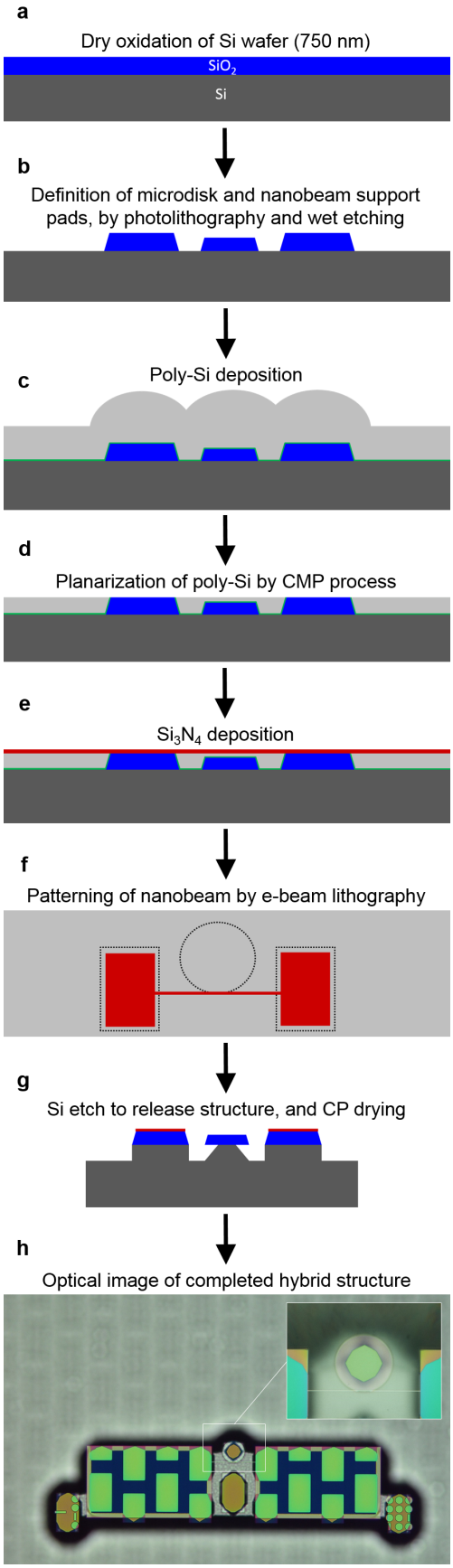

FIG. 6. Fabrication process flow: blue, red, green, and (light) gray indicate SiO_2, Si_3N_4, Al_2O_3, and (poly-)Si, respectively.

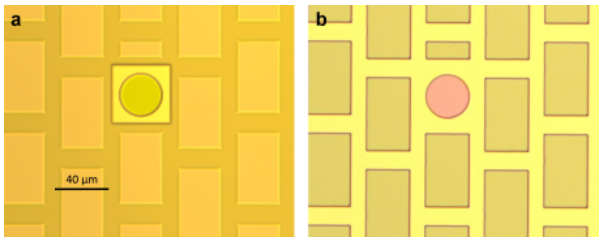

FIG. 7. Defining the vertical gap between the disk and the nanobeam: (a) Top view of patterned SiO_2 prior to selective etch of the microdisk. Photoresist protects the sacrificial structures, while a window is exposed around the microdisk. (b) Top view after selective etch of the microdisk and removal of the photoresist. The altered color of the microdisk indicates thinning.

until it is 10-100 nm thinner than the surrounding pads (later defining the beam-disk gap). The result, after the photoresist is stripped, is shown in Fig. 7b. Note that the microdisk reflects a different color than the surrounding pads due to its reduced thickness. Also seen in Fig. 7 is a matrix of sacrificial pads surrounding the disk. This matrix extends across the entire wafer and is only broken where microdisks or alignment marks (not shown) are placed. As discussed in Sec. III B, a uniform matrix of pads is necessary to achieve a flat surface when chemical mechanical polishing the sacrificial layer.

The final result of microdisk fabrication is illustrated in Fig. 6b. Blue indicates (in profile) the patterned SiO_2 film, with the microdisk in the center and nanobeam support pads on either side. The offset between the microdisk and the pads is highlighted with a dashed line. Not shown are sacrificial pillars and alignment marks. In the next processing step, all structures are buried in a sacrificial layer, onto which a Si_3N_4 film will be grown.

B. Planarized sacrificial layer

After patterning, the SiO_2 film is covered with a layer of sacrificial material. The sacrificial layer is used as a substrate for deposition and patterning of the Si_3N_4 film, meanwhile protecting the underlying microdisk. A crucial consideration is the thickness and flatness of the sacrifical layer, which is initially uneven because of its conformity to the underlying SiO_2 pattern. To thin and planarize the sacrificial layer, a delicate chemical-mechanical polishing (CMP) procedure is followed.

Poly-Si is chosen as the sacrifical material because it can be isotropically etched with high selectivity to SiO_2 and Si_3N_4, is well-suited to CMP, can withstand the high temperatures required for LPCVD Si_3N_4 ($> 800\,^{\circ}C$), and can be used to undercut the nanobeam and the microdisk in a single step. A 1.5 μm thick layer is deposited by LPCVD at $600\,^{\circ}C$ using silane and disilane as reactants. In addition, immediately before poly-Si deposition, a 5 nm aluminum oxide (Al_2O_3) film is deposited atop the SiO_2 using atomic layer deposition. This film later serves as an etch-stop to protect the microdisk when releasing the Si_3N_4 nanobeam. (Al_2O_3 etches over 100× slower than Si_3N_4 in flourine-based RIE used, and thus a few nanometers is sufficient to protect the microdisk.)

A profile of the pre-polished sacrificial layer is sketched in Fig. 6c. The Al_2O_3 etch-stop film is indicated by green. Immediately above the etch-stop is the layer of poly-Si (gray). Because of the underlying SiO_2 structures, the surface of the poly-Si is uneven. This surface is planarized by CMP before Si_3N_4 is deposited.

CMP involves pressing the wafer against a rotating polishing pad in the presence of an abrasive and corrosive chemical slurry. Abrasion is provided by SiO_2 particles 30-50 nm in diameter. The slurry PH is adjusted to achieve the desired polishing rate. In practice the polishing rate is also a function of applied force, rotation speed, and wafer topography. Areas of the wafer where features are sparse experience a higher pressure and thus a higher polishing rate than areas where features are dense. In order to reduce the poly-Si thickness to less than 100 nm over the entire 100 mm wafer, a uniform polishing rate is critical. This is the reason for patterning a matrix of sacrificial pads (Fig. 7).

The objective of the CMP process is to remove poly-Si until the pads are exposed, while maintaining a thin layer above the recessed microdisk (Fig. 6d). This procedure is complicated by the fact that the polishing rate varies across the wafer and, more importantly, that the polishing rate above the microdisk is faster than the rate above the adjacent nanobeam support pads. The latter results in a poly-Si layer which is thinner above the microdisk than at the nanobeam supports. To reduce this "dishing" effect, the support pads are brought as close the microdisk as possible (limited to 7 μm by photolithography and BHF biasing). To further reduce dishing, a two step polishing technique is used. First a slurry designed to etch poly-Si is used to remove the bulk of the material, leaving approximately 100 nm above the pads. The remaining material is removed with a slurry designed to etch SiO_2 faster than poly-Si. When the surface of the SiO_2 pads is reached, the dishing effect begins to reverse, resulting in an overall flat surface. We emphasize that the slurries used to polish poly-Si and SiO_2 are chemically distinct. The poly-Si slurry is basic (PH $\sim$ 11), while the SiO_2 slurry is neutral and uses smaller sized polishing particles. The former provides a more uniform polishing rate while the latter achieves a lower surface roughness ($\sim$ 0.3 nm RMS).

The gap between the microdisk and nanobeam is not determined by the thickness of the sacrificial layer, but rather by the pre-defined difference in thickness between the microdisk and the pads (Fig. 6b). During the final steps of CMP, however, the support pads are etched. The final gap is therefore smaller than originally defined by thinning of the microdisk. In order to precisely tune the gap, the thickness of the clamping pads is iteratively measured by reflectometry until a desired value is reached. The sample is then ready for Si_3N_4 deposition.

C. Nanobeam fabrication

To form the nanobeam, a 50-100 nm film of high-stress Si_3N_4 is deposited onto the planarized poly-Si layer. LPCVD is performed at $800\,^{\circ}C$ using dichlorosilane and ammonia, producing a nearly stoichiometric Si_3N_4. High stoichiometry is important for reducing absorption caused by hydrogen and oxygen impurities [54]. Moreover, the stress (800 MPa) resulting from high temperature deposition is important for achieving high mechanical quality factors [44].

To maximize optomechanical coupling, it is necessary to fine tune the lateral beam-disk separation with 100 nm precision (Fig. 5c). This is accomplished using e-

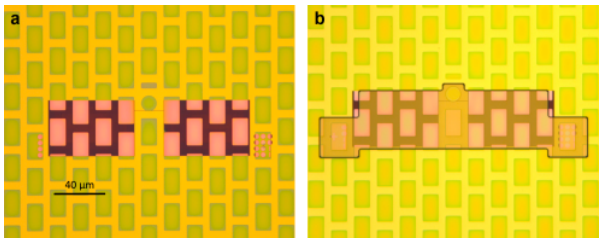

FIG. 8. Defining the nanobeam and the "mesa". (a) Top view of sample after etching of Si_3N_4 (pink and purple). Surrounding SiO_2 structures, including microdisk, appear green. (b) Image of the "mesa" photomask.

beam lithography to define the beams, in conjunction with the alignment markers defined during SiO_2 patterning. Importantly, after Si_3N_4 deposition, the markers are buried under Si_3N_4 and poly-Si, and cannot be seen by the electron-beam. A series of etch steps are used to locally uncover the markers; in addition, to improve contrast, the exposed markers are used as a hard mask to etch 2 μm into the underlying Si, using a highly selective flourine-based etch. The resulting high-contrast markers permit alignment of the Si_3N_4 mask with sub-100 nm precision.

The nanobeams, support pads, and sample labels are patterned in a 180 nm-thick hydrogen silsesquioxane (HSQ) negative photoresist. To reduce writing time, the pattern is separated into two parts, one containing the nanobeams and one containing the pads and labels. The former is written with a high resolution of 5 nm, while the latter is written with a 50 nm resolution. Proximity effect correction is used to ensure a high fidelity pattern. The e-beam pattern is transferred to Si_3N_4 using an SF_6 RIE etch. The resulting structure is shown in Fig. 8a.

D. Structural release

1. *Mesa and sample chip*

Before the nanobeam and microdisk are released, they are elevated from the surrounding wafer on a rectangular "mesa". This later enables alignment of a straight tapered optical fiber to the microdisk [62]. Figure 8b shows the mesa defined in a 5 μm mask of Microchemicals AZ 9260 photoresist. Flourine-based RIE is used to remove the surrounding poly-Si. The underlying sacrificial SiO_2 pads are removed by a subsequent BHF etch, exposing the Si substrate. To create the elevated mesa, exposed Si is recessed an additional 50 μm by RIE.

After releasing the mesa, the sample chips are defined. To define the sample chips, the wafer is coated with a protective photoresist layer and partially diced (300 μm deep) with a high precision Si dicing saw. Partial dicing is important as it leaves the wafer intact, enabling further processing using wafer-scale equipment. After partial dicing the photoresist is stripped, so that final release steps can be carried out.

2. *Nanobeam and microdisk*

To release the nanobeam and undercut the microdisk, the partially diced wafer is immersed in 40% KOH at 45 °C, selectively removing poly-Si but also etching Si. The etch time is fine-tuned with two opposing criteria in mind: (1) to ensure that the microdisk is undercut sufficiently far from its rim to avoid optical losses and (2) to ensure that Si underneath the nanobeam clamping point is not etched away. After KOH etching, the wafer is rinsed in water and any remaining potassium is neutralized in a bath of hydrochloric acid. Organic cleaning is then performed using an exothermic mixture of three parts sulfuric acid to one part 30% hydrogen peroxide (a "pirahna etch"). After rinsing again, the wafer is transfered directly to the ethanol bath of a critical point drying (CPD) machine. After CPD, the wafer is broken into sample chips along the partially diced lines, concluding the fabrication process.

IV. DEVICE CHARACTERIZATION

A. Experimental setup

Samples are characterized using the experimental setup shown in Fig. 9. Light from a $765-785$ nm tunable diode laser (New Focus Velocity 6312) is coupled into the microdisk using a tapered optical fiber (780 HP) [29]. The forward-scattered ("transmitted") field is monitored using one of two techniques: direct detection with an avalanche photodiode (Thorlabs APD110) and balanced homodyne detection with a pair of fast Si photodiodes (FEMTO HCA-S-100). DC- and AC-filtered photosignals are split between an oscilloscope (Tektronix DPO4034) and a spectrum analyzer (Tektronix RSA5106A). To calibrate laser-cavity detuning, a fraction of the input field is simultaneously passed through a 20-cm-long (FSR $\sim$ 350 MHz) fiber loop cavity. Optical decay rates are inferred from measurements of transmitted power versus laser detuning (Fig. 9b). Mechanical properties, including the optomechanical coupling rates, are inferred from measurements of thermomechanical cavity frequency noise [63] (Fig. 9c). To calibrate this noise, the input field is frequency modulated using an electro-optic modulator (EOSpace). Residual amplitude modulation — an important source of calibration error — is actively suppressed by stabilizing the phase of an out-of-loop heterodyne beat [64]. To eliminate gas damping of the nanobeam, the sample chip and the fiber coupling setup (based on an Attocube stack) are embedded in a vacuum chamber operating at $< 10^{-5}$ mbar.

B. Thermal noise measurement

Mechanical mode frequencies $\Omega_{\rm m}$, damping rates $\Gamma_{\rm m}$, and optomechanical coupling rates g_0, were determined by analyzing the cavity resonance frequency noise produced by thermal motion of the nanobeam. An in-depth description of this method is given in [63]. Important details are recounted below for clarity.

Thermal motion of the nanobeam $x(t)$ is written onto the cavity resonance frequency $\omega_c(t)$ via their optomechanical coupling, $G = d\omega_c/dx$. To measure $\omega_c(t)$, we monitor the power of the transmitted field while operating at a fixed detuning of $|\Delta| \approx \kappa/2$. Referred to the output voltage (V) of the photodetector transimpedance amplifier, the uncalibrated noise spectrum can be expressed as $S_V(\Omega) = |G_{V\omega}(\Omega)|^2 S_\omega(\Omega)$, where $G_{V\omega}(\Omega)$ is

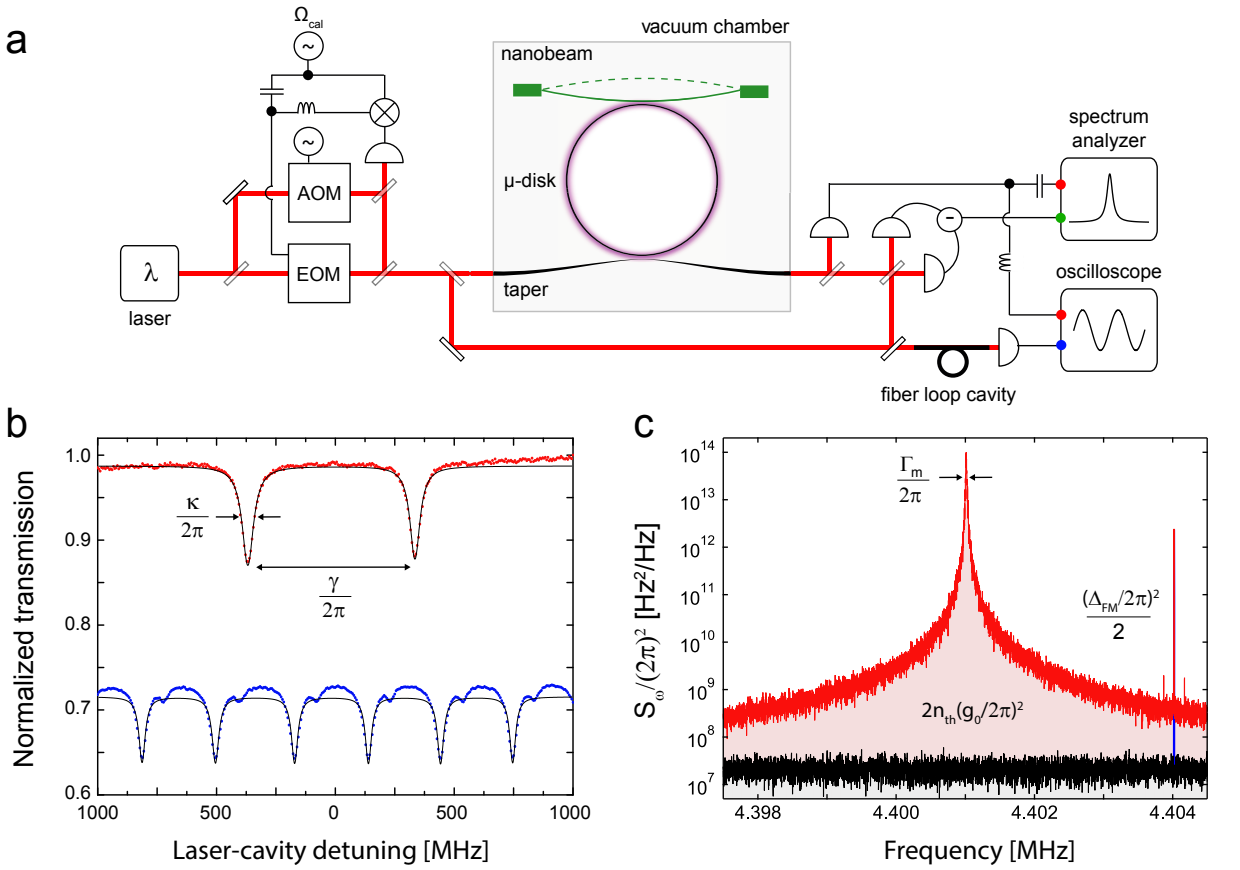

FIG. 9. (a) Overview of the experimental apparatus, described in Sec. IV A. (b) Representative optical Q measurement. WGM loss rates (κ) and mode splitting (γ) are inferred from the cavity transmission profile (red), generated by sweeping the diode laser frequency while monitoring the transmitted power. The sweep is calibrated by simultaneously monitoring transmission through a fiber loop cavity (blue). (c) Representative thermomechanical noise measurement. $\Omega_{\rm m}, \Gamma_{\rm th}$, and g_0 are inferred from the center frequency, linewidth, and area beneath the thermal noise peak (pink), respectively. The latter is calibrated by normalizing to the area beneath a FM tone (blue).

the measurement transfer function and $S_\omega(\Omega)$ is the apparent cavity frequency noise. $G_{V\omega}(\Omega)$ is calibrated by applying a phase modulation tone of known depth ($\beta_{\rm cal}$) and frequency ($\Omega_{\rm cal}$) to the input, resulting in a narrow spectral peak with area $|G_{V\omega}(\Omega_{\rm cal})|^2\beta_{\rm cal}^2\Omega_{\rm cal}^2/2$ [63].

A representative measurement is shown in Fig. 9c. Red, blue, and grey components correspond to thermal noise, $S_\omega^{\rm th}(\Omega)$, the calibration tone, $S_\omega^{\rm cal}(\Omega)$, and measurement imprecision, $S_\omega^{\rm imp}(\Omega)$, respectively. The full signal can be modeled as

$$S_\omega(\Omega) = S_\omega^{\rm th}(\Omega) + S_\omega^{\rm cal}(\Omega) + S_\omega^{\rm imp}(\Omega) \tag{3a}$$

$$\approx 2g_0^2 n_{\rm th}\cdot\mathcal{L}(\Omega-\Omega_{\rm m}) \tag{3b}$$

$$+\frac{\beta_{\rm cal}^2\Omega_{\rm cal}^2}{2}\cdot\mathcal{G}(\Omega-\Omega_{\rm cal}) + S_\omega^{\rm imp}(\Omega), \tag{3c}$$

where $\mathcal{L}(\Omega) = 4\Gamma_{\rm m}/(\Gamma_{\rm m}^2 + 4\Omega^2)$ is a normalized Lorentzian (characterizing the mechanical susceptibility) and $\mathcal{G}(\Omega) = e^{-\Omega^2/(2B^2)}/\sqrt{2\pi B^2}$ is a normalized Gaussian (characterizing the window function of the spectrum analyzer, which is assumed to have a resolution bandwidth $B \ll \Gamma_{\rm m}$). To calibrate the vertical axis in Fig. 9c, it is assumed that $|G_{V\omega}(\Omega_{\rm m})| \approx |G_{V\omega}(\Omega_{\rm cal})|$. Fitting the calibrated spectrum to Eq. 3 gives $\Omega_{\rm m}$, $\Gamma_{\rm m}$, and g_0. The last inference requires knowledge of $n_{\rm th}$. By using input powers low enough to neglect photothermal/radiation pressure damping (~ 10 nW), we assume that $n_{\rm th} \approx k_{\rm B}\cdot 295\ {\rm K}/(\hbar\Omega_{\rm m})$.

C. Optical spring effect

As a cross-check of the thermal noise measurement, g_0 was independently estimated from the optical spring effect [11]. In the experimentally relevant bad cavity limit ($\Omega_{\rm m} \ll \kappa$), the mechanical frequency shift produced by a radiation pressure optical spring is

$$\Delta\Omega_{\rm m}(\Delta) \approx \frac{8g_0^2}{\kappa}\cdot n_{\rm c}(\Delta)\cdot\frac{\Delta/\kappa}{1+4(\Delta/\kappa)^2} \tag{4}$$

where Δ is the laser-cavity detuning, $n_{\rm c}(\Delta) = (4P/(\hbar\omega_0\kappa))(\kappa_{\rm ex}/\kappa)/(1+4(\Delta/\kappa)^2)$ is the intracavity photon number, and P is the power injected into the cavity. (We note that radiation pressure damping also occurs for a detuned input field; however, in the devices studied, for which $\Omega_{\rm m}/\kappa \sim 0.01$, this effect was found to be overwhelmed by photothermal damping [65].)

A measurement of the optical spring effect is shown in Fig. 10, corresponding to the sample also characterized in Fig. 9c. The injected powers used — $P = 60, 120$ nW — were chosen to avoid instabilities due to photothermal/radiation pressure damping. The cavity was critically coupled ($\kappa_{\rm ex} \approx \kappa/2 \approx 2\pi\cdot 550$ MHz) and laser detuning was estimated from the mean transmitted power. Overlaid models correspond to Eq. 4 with the value $g_0 = 2\pi\cdot 60$ kHz, inferred from a least-squared fit to the low power measurement. This value is within

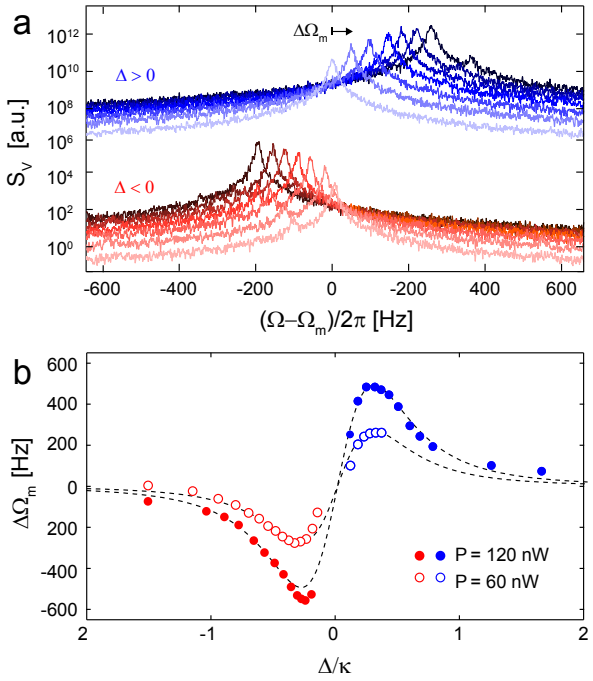

FIG. 10. Optical spring measurement. (a) Thermal noise spectrum of the fundamental beam mode as a function of laser detuning. Blue and red spectra indicated blue ($\Delta > 0$) and red ($\Delta < 0$) detuning, respectively. Lighter shades indicate smaller detuning. Blue spectra are vertically offset. (b) Plot of optical spring shift, $\Delta\Omega_{\rm m}$, versus normalized detuning, Δ/κ. Dashed black lines are a fit to Eq. 4 using g_0 as a free parameter.

10% of that inferred from thermal noise in Fig. 9c.

D. g_0 and $\mathcal{C}_0$ versus lateral beam position

As discussed in Sec. II C, g_0 depends sensitively on the lateral positioning of the nanobeam, and assumes a maximum (minimum) value for out-of-plane (in-plane) flexural modes when centered above the WGM. This behavior was studied by sweeping the lateral position of the beam using an appropriate e-beam mask (Sec. III C). Measurements of g_0 versus lateral beam position are shown in Fig. 11a. (In-plane modes exhibit typically $10\times$ lower g_0, and were not considered.) for beam and disk dimensions of $\{l, w, t\} = \{60, 0.4, 0.06\}$ μm and $\{r, t_{\rm d}, \theta\} = \{15\,\mu{\rm m}, 0.60\,\mu{\rm m}, 30\,{\rm deg.}\}$, respectively, and for a vertical gap of 25 nm. In agreement with numerical modelling (dashed line), g_0 assumes a maximum of $2\pi \cdot 40$ kHz as the outer edge of the beam eclipses the rim of the disk.

Also shown in Fig. 11b are measurements of κ versus lateral beam position (y). When the beam is displaced far from the disk, κ converges to the intrinsic value of $\sim 2\pi \cdot 100$ MHz observed in Fig. 4, suggesting that CMP did not significantly affect microdisk surface quality. As the beam is brought within 100 nm of the disk, κ is observed to increase sharply. The observed exponential dependence κ on y is independent of mode polarization and similar to the scaling observed in [35] with a beam coupled to a microtoroid. The absolute magnitude of the loss is also inconsistent with bulk Si_3N_4 optical absorption — specifically, accounting for the relatively small fraction of energy stored in the beam, the observed loss would require an imaginary index of $\sim 10^{-4}$, which is 1-2 orders of magnitude larger than conventionally observed for Si_3N_4 at NIR wavelengths [54, 66]. We thus conjecture that this loss is due to scattering from and/or waveguide coupling into the beam.

Combining measurements of g_0 and κ with typical room temperature mechanical damping rate of $\Gamma_{\rm m} = 2\pi \cdot 15$ Hz (we observed no change in $\Gamma_{\rm m}$ for small beam-disk seperation, suggesting that squeeze-film gas damping [53] was not a factor), the single-photon cooperativity is observed to approach $\mathcal{C}_0 \sim 1$. This value is limited by the unfavorable scaling of g_0^2/κ as g_0 begins to saturate. Despite this limitation, the inferred $\mathcal{C}_0$ represents a nearly 50 dB increase over our prior chip-scale implementation [34], owing to the combined 100-fold increase of g_0 and 10-fold reduction in κ. Increase g_0 is due to the precise vertical and lateral positioning of the beam afforded by CMP and e-beam processing. Reduced κ is due to greater isolation of the disk during beam patterning, making use of the poly-Si sacrificial layer. Fig. 11b suggests that κ is ultimately dominated by beam-induced scattering/absoption loss, rather than deterioration of intrinsic disk loss (Fig. 4), implying that an additional 10-fold reduction in κ may yet be realized with appropriate beam shaping/positioning.

E. g_0 and $\mathcal{C}_0$ versus beam width and disk thickness

Wider beams ($w \sim \lambda$) and thinner disks ($t_{\rm d} < \lambda$) were fabricated in an attempt to increase g_0 and $\mathcal{C}_0$ (see Eq. 2). Measurements of $\{g_0, \mathcal{C}_0\}$ vs w for two microdisk thicknesses, $t_{\rm d} \approx 0.43$ and 0.63 μm, are shown in Fig. 11. Fixed dimensions of the nanobeam and microdisk are $\{t, l\} \approx \{0.06, 60\}$ μm and $\{r_{\rm d}, \theta\} \approx \{15\ \mu{\rm m}, 30\ {\rm deg.}\}$, respectively. The lateral beam position was chosen to maximize g_0 for the 0.4 μm-wide beam (see Fig. 11). For the TE optical modes studied, a roughly $2\times$ increase in g_0 was observed for the 30% thinner disk. In both cases, g_0 scaled roughly linearly for widths $w \in [0.4, 1]$ μm. $\mathcal{C}_0$ also increased with w, roughly in proportion to g_0^2, for both $t_{\rm d}$. This is due to the fact that κ (not shown) was roughly independent of w for both disk thicknesses and a factor of four larger for the thinner disk. The highest optomechanical coupling rate we have measured, $g_0 \approx 2\pi \cdot 150$ Hz, was for a 1 μm-wide beam coupled to a 0.43 μm-thick disk. The highest cooperativities observed, $\mathcal{C}_0 > 2.5$, were for 1 μm-wide beams coupled to disks of both thicknesses.

F. g_0 versus mechanical mode order

g_0 was also studied for higher order mechanical modes. As shown in Fig. 11d , g_0 decreases as the vibrational node spacing approaches the dimensions of the effective sampling length $l_{\rm eff}$. In this case the model in Sec. II C — which assumes rigid displacement of a beam with effective mass $m = \rho t w l/2$ — breaks down. A simple extension of the model is shown as a red line in Fig. 11d. Here m is computed with respect to optical-intensity-

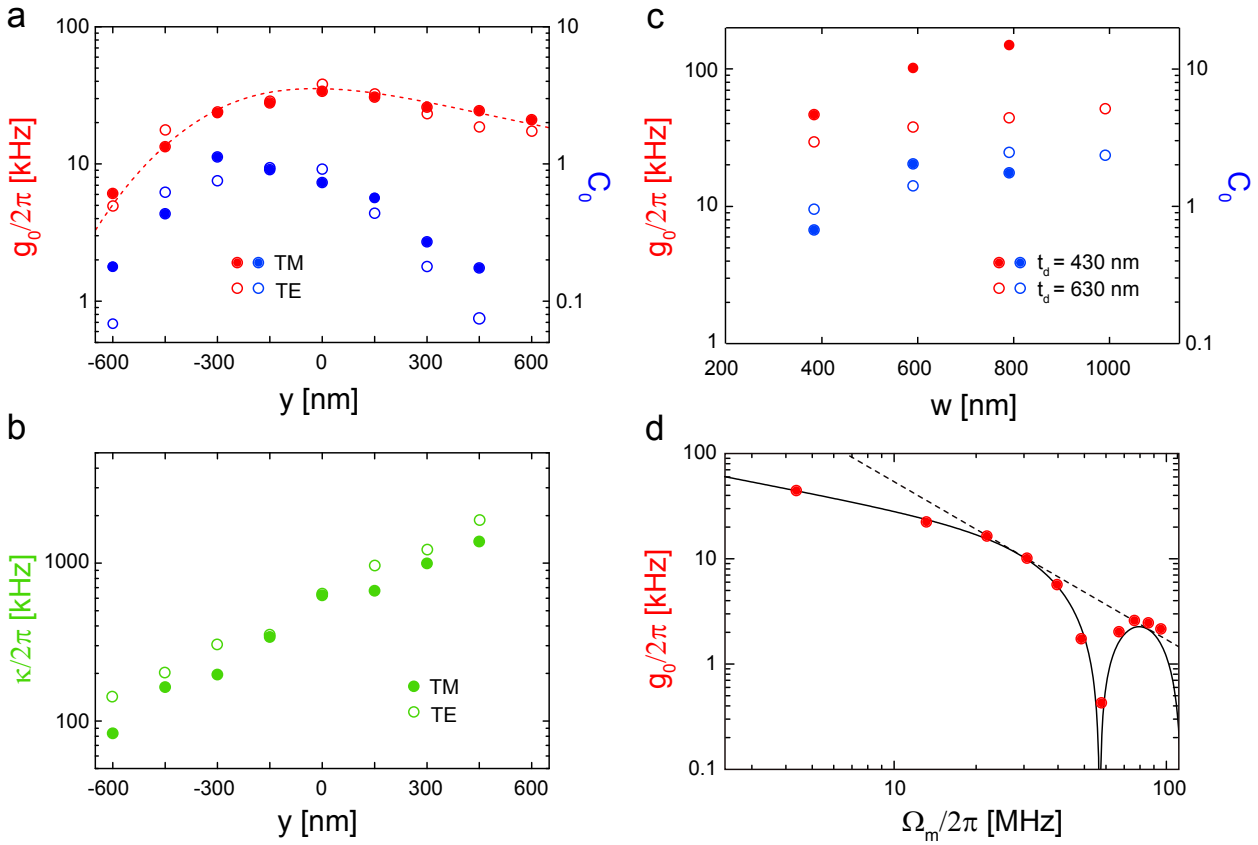

FIG. 11. (a) Measured vacuum optomechanical coupling rate (g_0) and cooperativity ($\mathcal{C}_0$, assuming $\Gamma_m = 2\pi \cdot 20$ Hz) versus lateral beam position (y) for TM (solid circles) and TE (open circles) cavity modes. (b) Corresponding intrinsic cavity decay rate (κ_0). (c) Measured g_0 versus beam width (w) for two disk thicknesses (t_d). (d) Measured g_0 versus mode frequency, $\Omega_m^{(n)} \approx n\Omega_m^{(0)}$. Red dots correspond to odd harmonics ($n = 1, 3, 5...$). Solid and dashed lines are model curves (Eq. 5b) for a sampling length of $l_{\rm eff} = 9.6$ and $l_{\rm eff} = 0$, respectively

weighted displacement of the mechanical mode:

$$m = \frac{\int_{\rm beam} \rho |u(r)|^2 d^3r}{|\int_{\rm beam} |E(r)|^2 u(r) d^3r / \int_{\rm beam} |E(r)|^2 d^3r|^2} \quad (5a)$$

$$\approx \frac{\rho t w l}{1-(-1)^n} \frac{1}{\mathrm{sinc}^2\left(\frac{n\pi}{2}\frac{l_{\rm eff}}{l}\right)} \quad (5b)$$

where $\vec{u}(x,y,z) \approx \sin(n\pi x/l)\hat{z}$ is the displacement profile of the $n^{\rm th}$-order out-of-plane flexural mode. The latter expression is appropriate when the transverse dimensions of the beam are much smaller than that of the WGM, and assumes that the intensity distribution sampled by the beam is uniform along the beam axis with an effective sampling length $l_{\rm eff}$. Using $\Omega_m \propto n$ gives $g_0^{(n)}/g_0^{(0)} \approx |\mathrm{sinc}\left(\frac{n\pi}{2}\frac{l_{\rm eff}}{l}\right)|/\sqrt{n}$ for odd n and 0 for even n. The model shown in Fig. 11d agrees quantitatively with experiment assuming an effective length of $l_{\rm eff} = 9.6$ μm as the only free parameter. A simple route to increasing g_0 would be to remove mass from the beam outside of the effective sampling length (see Fig. 13).

V. DISPLACEMENT SENSITIVITY

As an illustration of device performance, we use the microdisk to perform a cavity-enhanced interferometric measurement of the beam's displacement. For this purpose, the fiber taper and microdisk are embedded in one arm of a length- and power-balanced homodyne interferometer (Fig. 9). The cavity is driven on resonance using the Pound-Drever-Hall technique. A piezoelectric mirror is use to stabilize the interferometer path length difference so that the homodyne photocurrent is proportional to the phase of the transmitted cavity field.

Displacement noise spectra are shown in Fig. 12 for a $\{l, w, t\} = \{60, 0.4, 0.06\}$ μm beam with a vertical beam-disk separation of approximately 35 nm and optomechanical parameters $\{\Omega_m, \Gamma_m, \kappa, g_0, \mathcal{C}_0\} \approx \{2\pi \cdot 4.4\,\mathrm{MHz}, 2\pi \cdot 10\,\mathrm{Hz}, 2\pi \cdot 700\,\mathrm{MHz}, 2\pi \cdot 28\,\mathrm{kHz}, 0.45\}$. (Here κ corresponds to the critically-coupled cavity linewidth and other parameters correspond to the fundamental out-of-plane mechanical mode.) For the measurements shown, the cavity was critically coupled and the power of the input field was swept from 0.01 − 20 μW. The homodyne photocurrent noise spectrum is plotted in units relative to the signal produced by a phonon of displacement $2S_\omega^{\rm zp}(\Omega_m) \approx (2\pi \cdot 10\,\mathrm{kHz}/\sqrt{\mathrm{Hz}})^2$ (equivalent to $2S_x^{\rm zp}(\Omega_m) \approx (2\pi \cdot 8.9\,\mathrm{fm}/\sqrt{\mathrm{Hz}})^2$ assuming $x_{\rm zp} = 25$ fm). In these units, the magnitude of the fundamental thermal noise peak (neglecting photothermal or dynamical back-action) is equal to the effective thermal occupation $n_{\rm tot} \equiv S_\omega(\Omega_m)/(2S_\omega^{\rm zp}(\Omega_m) = n_{\rm th} + n_{\rm ba} + n_{\rm imp}$, where $n_{\rm th} \equiv S_\omega^{\rm th}(\Omega_m)/2S_\omega(\Omega_m)$ is the ambient bath occupation, $n_{\rm ba}$ is the effective thermal bath occupation associated with classical and quantum measurement back-action (radiation pressure shot noise), and $n_{\rm imp} \equiv S_\omega^{\rm imp}(\Omega_m)/2S_\omega^{\rm zp}(\Omega_m)$ is the apparent thermal occupation

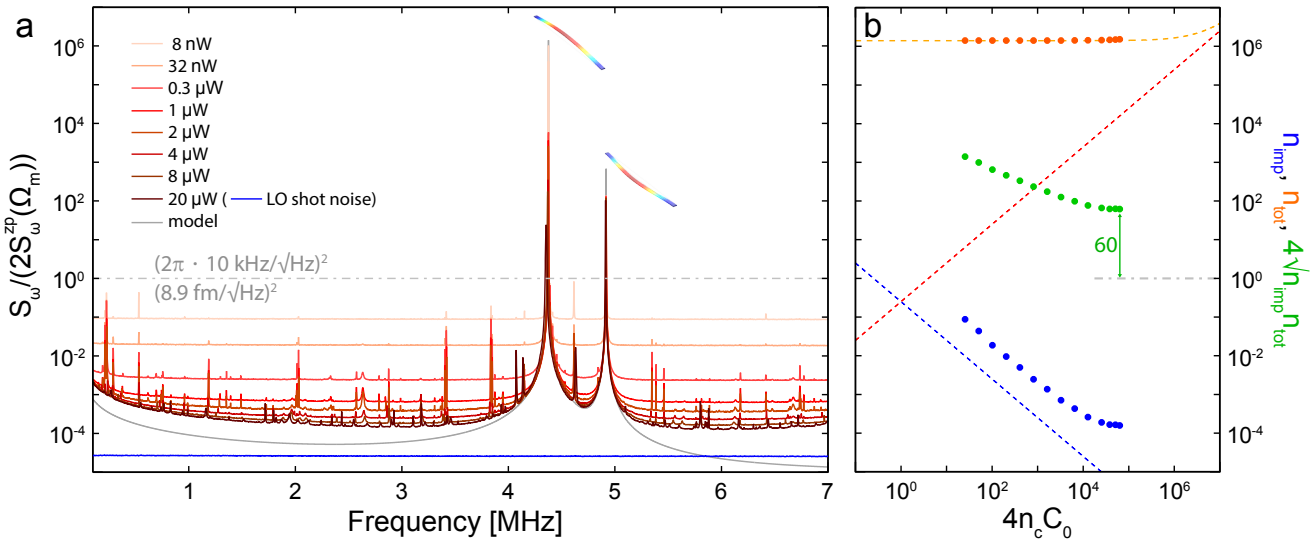

FIG. 12. (a) Nanobeam displacement noise, measured by balanced homodyne detection of the microdisk output field, for various input powers. Noise spectra are expressed in units relative to the cavity frequency noise produced by one phonon of fundamental out-of-plane vibration, $2S_\omega^{\rm zp}(\Omega_{\rm m}) = (2\pi \cdot 10\,{\rm kHz}/\sqrt{\rm Hz})^2$, where $\Omega_{\rm m} = 2\pi \cdot 4.4$ MHz. At large powers, the fundamental noise peak is shifted and broadened by optical spring softening and damping, respectively. The peak at 4.9 MHz is due to thermal motion of the fundamental in-plane mode. The gray curve is a model for the intrinsic thermal motion of the fundamental out-of-plane and in-plane modes (Eq. 6). (b) Measured phonon equivalent displacement, $n_{\rm tot} = S_\omega(\Omega_{\rm m})/2S_\omega^{\rm zp}(\Omega_{\rm m})$, displacement imprecision, $n_{\rm imp} \equiv S_\omega^{\rm imp}(\Omega_{\rm m})/2S_\omega^{\rm zp}(\Omega_{\rm m})$, and their geometric mean versus intracavity photon number $n_{\rm c}$ weighted by single-photon cooperativity $\mathcal{C}_0$. Dashed lines denote ideal values for $n_{\rm tot} = n_{\rm th} + n_{\rm ba} + n_{\rm imp}$ (orange), $n_{\rm ba} = \mathcal{C}_0 n_{\rm c}$ (red), and $n_{\rm imp} = 1/16\mathcal{C}_0 n_{\rm c}$ (blue), using $n_{\rm th} \approx 1.4 \cdot 10^6$ and $\mathcal{C}_0 = 0.45$. Green arrow indicates proximity to the uncertainty limit, $4\sqrt{n_{\rm imp} n_{\rm tot}} \geq 1$.

associated with the measurement imprecision. The noise spectra are calibrated by bootstrapping a low power measurement to $n_{\rm tot} \approx n_{\rm th} \approx k_{\rm B}T/\hbar\Omega_{\rm m} \approx 1.4 \cdot 10^6$ (for larger optical powers, dynamic spring/damping forces modify the peak value, $S_\omega(\Omega_{\rm m})$). At the highest optical powers, the displacement imprecision in the vicinity of $\Omega_{\rm m}$ is estimated (from the saddle at 2.5 MHz) to be $n_{\rm imp} \approx 1.5 \cdot 10^{-4}$, while the shot-noise imprecision (blue curve, obtained by decoupling the fiber from the cavity) is $n_{\rm imp}^{\rm (shot)} \approx 2.6 \cdot 10^{-5}$. These correspond to imprecisions 32 and 40 dB below that at the SQL ($n_{\rm imp} = 0.25$), respectively. The magnitude of the extraneous imprecision, $2S_\omega^{\rm zp}(\Omega_{\rm m}) \cdot (n_{\rm imp} - n_{\rm imp}^{\rm (shot)}) \approx (2\pi \cdot 110\,{\rm Hz}/\sqrt{\rm Hz})^2$, is independent of optical power and gives rise to the saturation of the blue points in 12b. This extraneous noise is consistent with a mixture of diode laser frequency noise ($\sim 30\,{\rm Hz}/\sqrt{\rm Hz}$ [18]), thermorefractive noise ($\sim 10\,{\rm Hz}/\sqrt{\rm Hz}$ [30]), and off-resonant thermal noise ($\sim 70\,{\rm Hz}/\sqrt{\rm Hz}$). The latter is estimated using the 'structural damping' model of Saulson [67],

$$\frac{S_\omega(\Omega)}{2S_\omega^{\rm zp}(\Omega_{\rm m})} \approx n_{\rm th}\frac{\Omega_{\rm m}}{\Omega}\frac{\Gamma_{\rm m}^2\Omega_{\rm m}^2}{(\Omega^2-\Omega_{\rm m}^2)^2+\Gamma_{\rm m}^2\Omega_{\rm m}^2} \gtrsim \frac{7n_{\rm th}}{Q_{\rm m}^2}, \quad (6)$$

shown in gray in Fig. 12, for $Q_{\rm m} = \Omega_{\rm m}/\Gamma_{\rm m} = 4.4 \cdot 10^5$.

The total efficiency of the measurement is estimated by comparing the power dependence of the imprecision ($n_{\rm imp}$), the effective thermal bath occupation ($n_{\rm tot}$), and their geometric mean $\sqrt{n_{\rm imp} n_{\rm tot}}$ to the ideal values $1/(16\mathcal{C}_0 n_{\rm c})$, $\mathcal{C}_0 n_{\rm c}$, and $1/4$, respectively, where the last case represents the Heisenberg uncertainty limit. As shown on the right hand side of Fig. 12, the imprecision is a factor of 7.5 larger than ideal, due to a combination of cavity loss (50%, corresponding to critical coupling), taper loss ($\sim 10\%$), homodyne detector loss/misalignment, and optical mode splitting [18]. The effective thermal bath occupation is inferred by fitting to the off-resonant tail of the fundamental noise peak (to avoid the systematic error due to optical damping). From these fits we infer a heating of $C_0^{\rm ext} \equiv (n_{\rm tot} - n_{\rm th})/n_{\rm c} = 1.4$, two times larger than expected due to quantum measurement back-action. The imprecision-back-action product is contrained, at high powers, to $4\sqrt{n_{\rm imp} n_{\rm tot}} \approx 60$, due to the saturation of the measurement imprecision. To the best of our knowledge, this represents the closest approach to the uncertainty limit for a room temperature mechanical oscillator.

VI. SUMMARY AND OUTLOOK

We have presented a method to heterogeneously integrate a high-stress, Si_3N_4 nanobeam within the evanescent near-field of a SiO_2 microdisk. Building on earlier strategies [30, 34], the principle advance is a fabrication technique which preserves the high Q/(mode volume) ratio of each resonator while enabling the beam and the disk to be separated by a vacuum gap of 10-100 nm — significantly smaller than the evanescent decay length of the optical mode. Samples of various dimensions were fabricated and characterized. Simultaneously low mechanical loss, $\Gamma_{\rm m} = 2\pi \cdot (10 - 100)$ Hz, low optical loss, $\kappa = 2\pi \cdot (100 - 1000)$ MHz, and large optomechanical coupling rates, $g_0 = 2\pi \cdot (10 - 100)$ kHz, were measured, corresponding to room temperature single-photon cooperativities as high as $\mathcal{C}_0 \equiv 4g_0^2/\Gamma_{\rm m}\kappa = 2$.

The reported system holds particular promise as a quantum-limited displacement sensor, owing to the large vacuum displacement of the nanobeam and the high power handling capacity of the microdisk. For

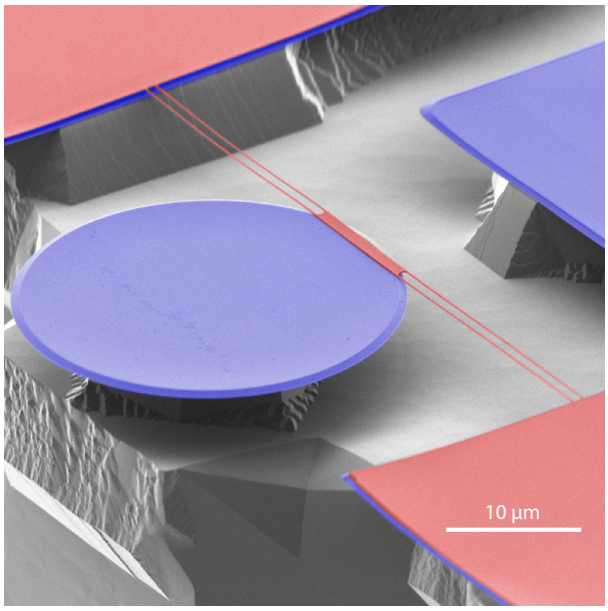

FIG. 13. Variation on a theme: suspending the nanobeam from tethers enables higer g_0 by reducing mass without changing optomechanical mode overlap. Here the central beam coincides with the effective sampling length of the optical mode.

a typical device, possessing $\{\Omega_m, \Gamma_m, \kappa_0, g_0\} \approx 2\pi \cdot \{4.5\text{ MHz}, 15\text{ Hz}, 500\text{ MHz}, 50\text{ kHz}\}$, the resonant vacuum displacement noise, $S_\omega^{zp}(\Omega_m) = 4g_0^2/\Gamma_m \approx (2\pi \cdot 26\text{ kHz}/\sqrt{\text{Hz}})^2$, is orders of magnitude larger than major sources of imprecision — such as laser frequency and thermorefractive noise [35] — and commensurate with shot noise for an ultra-low intracavity photon number of $n_c = 1/(16\mathcal{C}_0) = 0.05$ [18]. Operating a similar device at 4 K with $n_c \sim 10^5$ (corresponding to $P \sim 100\ \mu$W when critically coupled to the fiber waveguide), we were recently able to achieve a displacement imprecision n_{th} times (43 dB) below S_ω^{zp}, while maintaining an imprecision-back-action product within a factor of 5 of the uncertainty limit [18]. This regime of 'efficient' measurement — characterized by the ability to resolve a phonon-equivalent displacement in the thermal decoherence time — enabled us to feedback-cool the mechanical mode to near its ground state [18], and might be extended to other quantum control tasks, such as squeezed-state preparation [23].

An intriguing question is whether the reported device may be used to realize Heisenberg-limited displacment measurements at room temperature — namely, an apparent imprecision-back-action product $(n_{ba} + n_{th}) \cdot n_{imp} \to 1/4$ (see Sec. V). For the radio frequency oscillators under study ($n_{th} \sim 10^6$), the main challenges are (1) pumping the cavity with $n_c = n_{th}/C_0 \sim 10^6$ photons in order to achieve the necessary measurement strength (characterized by a phonon-equivalent RPSN of $n_{ba} = \mathcal{C}_0 n_c > n_{th}$), (2) reducing extraneous sources of measurement imprecision to $S_\omega^{zp}/n_{th} < (2\pi \cdot 10\text{ Hz}/\sqrt{\text{Hz}})^2$, and (3) reducing extraneous heating to ensure that n_{ba} is dominated by RPSN. Because of the (blue-stable) thermal self-locking effect in room temperature SiO_2 microresonators [68], the first requirement is expected to be limited by parametric radiation pressure instabilities, requiring active feedback damping. The second requirement — for microdisks with dimensions studied here — is expected to be limited by thermorefractive noise at the level of $S_\omega^{trn} \sim (2\pi \cdot 10\text{ Hz}/\sqrt{\text{Hz}})^2$ [35], an impressive 60 dB lower than S_ω^{zp}. Reaching $S_\omega^{trn} < S_\omega^{zp}/n_{th}$ would require a moderate increase in $g_0^2 \cdot Q_m$ (for instance, by using lower-mass, "tethered" beams [19]; see Fig. 13). The third requirement depends on the details of the nanoscale heat transfer process. At 4 K, we have observed photothermal heating consistent with an extraneous cooperativity of $\mathcal{C}_0^{ext} \equiv n_{ba}^{ext}/n_c \sim 1$ [18]; we anticipate this heating to reduce to tenable levels ($\mathcal{C}_0^{ext} < \mathcal{C}_0$) at room temperature, provided that the underlying process is related to the temperature-dependent thermal conductivity of amorphous glass [46]. Preliminary room temperature measurements, discussed in Sec. V, suggest that $\mathcal{C}_0^{ext} \sim \mathcal{C}_0$ can be met for a moderate $\mathcal{C}_0 \sim 0.8$.

In addition to high cooperativity, the evanescent sensing platform and reported fabrication method have as a compelling feature the ability to incorporate new materials and/or planar geometries above a high-Q microdisk with nanometric precision. This capability opens the door to a variety of "hybrid" sensing applications. For example, the system may be electrically functionalized by vertically integrating the beam into a parallel plate capacitor, or into the gradient field between two closely spaced electrodes [69]. This interface — which need not compromise the mechanical quality of the beam [70] — can form the basic building block of a high-efficiency electro-optic converter, with applications such as precision radio wave sensing [71]. Pushed to a different extreme, two dimensional materials such as graphene or MoS_2 may be integrated with a microdisk by using the SiN film as a sacrificial substrate [72]. Another intriguing possibility, in conjunction with the preparation of low entropy mechanical states using measurement-based feedback, is to functionalize the beam with a two-level system, such as an NV center embedded in a diamond nanocrystal [73]. Nanobeams integrated with microdisks may also serve as a platform for remotely-coupled "atom-optomechanics" [74, 75], taking advantage of the low oscillator mass, high cavity finesse, and recent developments in fiber-based atom traps [76]. In addition, we note that the ability to perform broadband, thermal-noise-limited measurements of high-Q nanomechanical oscillators (c.f. Fig. 12) may help shed light on the microscopic origin of intrinsic damping [77].

Finally, we remark that while our discussion has focused on quantum (imprecision and back-action) noise in the measurement of nanomechanical motion, nanomechanical sensors of mass/force/charge are in fact fundamentally limited by thermal motion. For such applications, the practical utility of the reported high-cooperativity evanescent sensing platform lies in the ability to resolve thermal motion with high signal-to-noise and large bandwidth for devices with widely-varying in-plane geometry. (By contrast, thermal motion in MEMS sensors is typically masked by Johnson noise.) [78]. This might enable, for instance, precision force sensors based on high-Q nanomechanical beam oscillators [34] or chip-scale accelerometers based on membrane-like micromechanical test masses [79]. For the nanobeam displacement measurements shown in Fig. 12, thermal noise is resolved over a bandwidth of $\sim$ MHz at the level of $4k_B T\Gamma_m m \sim (100\,\text{aN}/\sqrt{\text{Hz}})^2$ employing $\sim 10\,\mu$W of injected optical power. Notably, a moderate reduction in extraneous imprecision would enable thermal noise to be resolved over a full octave, a difficult challenge for high-Q resonators as it requires resolving the thermal peak with a signal-to-noise of $\sim Q^2$ (Eq. 6).

ACKNOWLEDGEMENTS

We acknowledge fabrication advice from E. Gavartin in early stages of the project. All samples were fabricated at the CMi (Center for Micro-Nanotechnology) at EPFL. Research was funded by an ERC Advanced Grant (QuREM), by the DARPA/MTO ORCHID programme, the Marie Curie Initial Training Network Cavity Quantum Optomechanics (cQOM), the Swiss National Science Foundation and through support from the NCCR of Quantum Engineering (QSIT). D.J.W. acknowledges support from the European Commission through a Marie Skodowska-Curie Fellowship (IIF project 331985).

[1] K. L. Ekinci and M. L. Roukes, Nanoelectromechanical systems, Rev. Sci. Instru. **76**, 061101 (2005).

[2] A. N. Cleland and M. L. Roukes, A nanometre-scale mechanical electrometer, Nature **392**, 160–162 (1998).

[3] H. J. Mamin and D. Rugar, Sub-attonewton force detection at millikelvin temperatures, App. Phys. Lett. **79**, 3358–3360 (2001).

[4] K Jensen, Kwanpyo Kim, and A Zettl, An atomic-resolution nanomechanical mass sensor, Nature Nano. **3**, 533–537 (2008).

[5] K. C. Schwab and M. L. Roukes, Putting mechanics into quantum mechanics, Physics Today **58**, 36–42 (2005).

[6] M. D. LaHaye, Approaching the quantum limit of a nanomechanical resonator, Science **304**, 74–77 (2004).

[7] N. E. Flowers-Jacobs, D. R. Schmidt, and K. W. Lehnert, Intrinsic noise properties of atomic point contact displacement detectors, Phys. Rev. Lett. **98**, 096804 (2007).

[8] C. A. Regal, J. D. Teufel, and K. W. Lehnert, Measuring nanomechanical motion with a microwave cavity interferometer, Nat. Phys. **4**, 555–560 (2008).

[9] J. D. Teufel, D. Li, M. S. Allman, K. Cicak, A. J. Sirois, J. D. Whittaker, and R. W. Simmonds, Circuit cavity electromechanics in the strong-coupling regime, Nature **471**, 204–208 (2011).

[10] T. J. Kippenberg and K. J. Vahala, Cavity optomechanics: back-action at the mesoscale, Science **321**, 1172–1176 (2008).

[11] M. Aspelmeyer, T. J. Kippenberg, and F. Marquardt, Cavity optomechanics, Rev. Mod. Phys. **86**, 1391–1452 (2014).

[12] C. M. Caves, Quantum-mechanical radiation-pressure fluctuations in an interferometer, Phys. Rev. Lett. **45**, 7579 (1980).

[13] J. Chan, T. P. Mayer Alegre, A. H.. Safavi-Naeini, J. T. Hill, A. Krause, S. Groeblacher, M. Aspelmeyer, and O. Painter, Laser cooling of a nanomechanical oscillator into its quantum ground state, Nature **478**, 89–92 (2011).

[14] E. Verhagen, S. Deléglise, S. Weis, A. Schliesser, and T. J. Kippenberg, Quantum-coherent coupling of a mechanical oscillator to an optical cavity mode, Nature **482**, 63–67 (2012).

[15] Teufel, J. D. et. al., Sideband cooling of micromechanical motion to the quantum ground state, Nature **475**, 359–363 (2011).

[16] I. Wilson-Rae, N. Nooshi, W. Zwerger, and T. J. Kippenberg, Theory of ground state cooling of a mechanical oscillator using dynamical backaction, Phys. Rev. Lett. **99**, 093901 (2007).

[17] V. B. Braginsky, F. Y. Khalili, and K. S. Thorne, *Quantum measurement* (Cambridge University Press, 1995).

[18] D. J. Wilson, V. Sudhir, N. Piro, R. Schilling, A. H. Ghadimi, and T. J. Kippenberg, Measurement-based control of a mechanical oscillator at its thermal decoherence rate, Nature **524**, 325–329 (2015).

[19] A. G Krause, T. D. Blasius, and O. Painter, Optical read out and feedback cooling of a nanostring optomechanical cavity, arXiv preprint arXiv:1506.01249 (2015).

[20] T. P. Purdy, R. W. Peterson, and C. A. Regal, Observation of radiation pressure shot noise on a macroscopic object, Science **339**, 801–804 (2013).

[21] J. D. Teufel, F. Lecocq, and R. W. Simmonds, Overwhelming thermomechanical motion with microwave radiation pressure shot noise, Phys. Rev. Lett. **116**, 013602 (2016).

[22] J.-M. Courty, A. Heidmann, and M. Pinard, Quantum limits of cold damping with optomechanical coupling, Eur. Phys. J. D **17**, 399408 (2001).

[23] A. Szorkovszky, A. C. Doherty, G. I. Harris, and W. P. Bowen, Mechanical squeezing via parametric amplification and weak measurement, Phys. Rev. Lett. **107**, 213603 (2011).

[24] D. Kleckner and D. Bouwmeester, Sub-kelvin optical cooling of a micromechanical resonator, Nature **444**, 75–78 (2006).

[25] J. D. Thompson, B. M. Zwickl, A. M. Jayich, Florian Marquardt, S. M. Girvin, and J. G. E. Harris, Strong dispersive coupling of a high-finesse cavity to a micromechanical membrane, Nature **452**, 72–75 (2008).

[26] A. Schliesser, G. Anetsberger, R. Rivire, O. Arcizet, and T. J. Kippenberg, High-sensitivity monitoring of micromechanical vibration using optical whispering gallery mode resonators, New J. Phys. **10**, 095015 (2008).

[27] M. Eichenfield, J. Chan, Ryan M. Camacho, K. J.. Vahala, and O. Painter, Optomechanical crystals, Nature **462**, 78–82 (2009).

[28] D. Van Thourhout and J. Roels, Optomechanical device actuation through the optical gradient force, Nat. Phot. **4**, 211–217 (2010).

[29] S. M. Spillane, T. J. Kippenberg, O. J. Painter, and K. J. Vahala, Ideality in a fiber-taper-coupled microresonator system for application to cavity quantum electrodynamics, Phys. Rev. Lett. **91**, 043902 (2003).

[30] G. Anetsberger, O. Arcizet, Q. P. Unterreithmeier, R. Rivire, A. Schliesser, E. M. Weig, J. P. Kotthaus, and T. J. Kippenberg, Near-field cavity optomechanics with nanomechanical oscillators, Nat. Phys. **5**, 909–914 (2009).

[31] C. Doolin, P. H. Kim, B. D. Hauer, A. J. R. MacDonald, and J. P. Davis, Multidimensional optomechanical cantilevers for high-frequency force sensing, New J. Phys. **16**, 035001 (2014).

[32] R. M. Cole, G. A. Brawley, V. P. Adiga, R. De Alba,

J. M. Parpia, B. Ilic, H. G. Craighead, and W. P. Bowen, Evanescent-field optical readout of graphene mechanical motion at room temperature, Phys. Rev. App. **3**, 024004 (2015).
[33] L. Neuhaus, E. van Brackel, E. Gavartin, P. Verlot, and T. J. Kippenberg, A versatile scheme for read-out and actuation of nanomechanical motion using silica microspheres, in *CLEO: Science and Innovations* (Optical Society of America, 2012) pp. CW3M–2.
[34] E. Gavartin, P. Verlot, and T. J. Kippenberg, A hybrid on-chip optomechanical transducer for ultrasensitive force measurements, Nat. Nano. **7**, 509–514 (2012).
[35] G. Anetsberger, E. Gavartin, O. Arcizet, Q. P. Unterreithmeier, E. M. Weig, M. L. Gorodetsky, J. P. Kotthaus, and T. J. Kippenberg, Measuring nanomechanical motion with an imprecision below the standard quantum limit, Phys. Rev. A **82** (2010).
[36] R. A. Norte, J. P. Moura, and S. Gröblacher, Mechanical resonators for quantum optomechanics experiments at room temperature, Phys. Rev. Lett. **116**, 147202 (2016).
[37] A. H. Safavi-Naeini, S. Groeblacher, J. T. Hill, J. Chan, M. Aspelmeyer, and O. Painter, Squeezed light from a silicon micromechanical resonator, Nature **500**, 185–189 (2013).
[38] T. P. Purdy, P.-L. Yu, R. W. Peterson, N. S. Kampel, and C. A. Regal, Strong optomechanical squeezing of light, Phys. Rev. X **3** (2013).
[39] R. Leijssen and E. Verhagen, Strong optomechanical interactions in a sliced photonic crystal nanobeam. Sci. Rep. (2015).
[40] E. E. Wollman, C. U. Lei, A. J. Weinstein, J. Suh, A. Kronwald, F. Marquardt, A. A. Clerk, and K. C. Schwab, Quantum squeezing of motion in a mechanical resonator, Science **349**, 952–955 (2015).
[41] T. A. Palomaki, J. W. Harlow, J. D. Teufel, R. W. Simmonds, and K. W. Lehnert, Coherent state transfer between itinerant microwave fields and a mechanical oscillator, Nature **495**, 210–214 (2013).
[42] M. Wu, A. C. Hryciw, C. Healey, D. P. Lake, H. Jayakumar, M. R. Freeman, J. P. Davis, and P. E. Barclay, Dissipative and dispersive optomechanics in a nanocavity torque sensor, Phys. Rev. X **4**, 021052 (2014).
[43] N. Matsumoto, K. Komori, Y. Michimura, G. Hayase, Y. Aso, and K. Tsubono, 5-mg suspended mirror driven by measurement-induced backaction, Phys. Rev. A **92**, 033825 (2015).
[44] S. S. Verbridge, J. M. Parpia, Rob. B. Reichenbach, L. M. Bellan, and H. G. Craighead, High quality factor resonance at room temperature with nanostrings under high tensile stress, J. Appl. Phys. **99**, 124304 (2006).
[45] M. Imboden and P. Mohanty, Dissipation in nanoelectromechanical systems, Phys. Rep. **534**, 89–146 (2014).
[46] R. O. Pohl, X. Liu, and E. J. Thompson, Low-temperature thermal conductivity and acoustic attenuation in amorphous solids, Rev. Mod. Phys. **74**, 991 (2002).
[47] L. G. Villanueva and S. Schmid, Evidence of surface loss as ubiquitous limiting damping mechanism in sin micro-and nanomechanical resonators, Phys. Rev. Lett. **113**, 227201 (2014).
[48] J. Rieger, A. Isacsson, M. J. Seitner, J. P. Kotthaus, and E. M. Weig, Energy losses of nanomechanical resonators induced by atomic force microscopy-controlled mechanical impedance mismatching, Nat. Comm. **5** (2014).
[49] G. I. González and P. R. Saulson, Brownian motion of a mass suspended by an anelastic wire, J. Acoust. Soc. Am. **96**, 207–212 (1994).
[50] Q. P. Unterreithmeier, T. Faust, and J. P. Kotthaus, Damping of nanomechanical resonators, Phys. Rev. Lett. **105**, 027205 (2010).
[51] A. H. Ghadimi, D. J. Wilson, and T. J. Kippenberg, Dissipation engineering of high-stress silicon nitride nanobeams, arXiv preprint arXiv:1603.01605 (2016).
[52] J. D. Teufel, T. Donner, M. A. Castellanos-Beltran, J. W. Harlow, and K. W. Lehnert, Nanomechanical motion measured with an imprecision below that at the standard quantum limit, Nat. Nano. **4**, 820–823 (2009).
[53] S. S. Verbridge, R. Ilic, H. G. Craighead, and J. M. Parpia, Size and frequency dependent gas damping of nanomechanical resonators, App. Phys. Lett. **93**, 013101 (2008).
[54] B. M. Zwickl, W. E. Shanks, A. M. Jayich, C. Yang, A. C. Bleszynski Jayich, J. D. Thompson, and J. G. E. Harris, High quality mechanical and optical properties of commercial silicon nitride membranes, Appl. Phys. Lett. **92**, 103125 (2008).
[55] T. J. Kippenberg, J. Kalkman, A. Polman, and K. J. Vahala, Demonstration of an erbium-doped microdisk laser on a silicon chip, Phys. Rev. A **74**, 051802 (2006).
[56] H. Lee, T. Chen, J. Li, K. Y. Yang, S. Jeon, O. Painter, and K. J. Vahala, Chemically etched ultrahigh-q wedge-resonator on a silicon chip, Nat. Phot. **6**, 369–373 (2012).
[57] T. J. Kippenberg, J. Kalkman, A. Polman, and K. Vahala, Demonstration of an erbium-doped microdisk laser on a silicon chip, Phys. Rev. A **74** (2006).
[58] M. Oxborrow, How to simulate the whispering-gallery modes of dielectric microresonators in femlab/comsol, in *Lasers and Applications in Science and Engineering* (International Society for Optics and Photonics, 2007) pp. 64520J–64520J.
[59] M. Borselli, T. Johnson, and O. Painter, Beyond the rayleigh scattering limit in high-q silicon microdisks: theory and experiment, Opt. Express **13**, 1515–1530 (2005).
[60] M. L. Povinelli, M. Loncar, M. Ibanescu, E. J. Smythe, S. G. Johnson, F. Capasso, and J. D. Joannopoulos, Evanescent-wave bonding between optical waveguides, Opt. Lett. **30**, 3042–3044 (2005).
[61] G. Anetsberger, *Novel cavity optomechanical systems at the micro-and nanoscale and quantum measurements of nanomechanical oscillators*, Ph.D. thesis, LMU Munich (2010).
[62] R. Riviere, O. Arcizet, A. Schliesser, and T. J. Kippenberg, Evanescent straight tapered-fiber coupling of ultra-high q optomechanical micro-resonators in a low-vibration helium-4 exchange-gas cryostat, Rev. Sci. Instrum. **84**, 043108 (2013).
[63] M. L. Gorodetsky, A. Schliesser, G. Anetsberger, S. Deleglise, and T. J.. Kippenberg, Determination of the vacuum optomechanical coupling rate using frequency noise calibration, Opt. Exp. **18**, 23236 (2010).

[64] W. Zhang, M. J. Martin, C. Benko, J. L. Hall, J. Ye, C. Hagemann, T. Legero, U. Sterr, F. Riehle, G. D. Cole, *et al.*, Reduction of residual amplitude modulation to 1× 10-6 for frequency modulation and laser stabilization, Opt. Lett. **39**, 1980–1983 (2014).

[65] C. H. Metzger and K. Karrai, Cavity cooling of a microlever, Nature **432**, 1002–1005 (2004).

[66] D. J. Wilson, C. A. Regal, S. B. Papp, and H. J. Kimble, Cavity optomechanics with stoichiometric sin films, Phys. Rev. Lett. **103**, 207204 (2009).

[67] P. R. Saulson, Thermal noise in mechanical experiments, Phys. Rev. D **42**, 2437 (1990).

[68] O. Arcizet, R. Rivière, A. Schliesser, G. Anetsberger, and T. J. Kippenberg, Cryogenic properties of optomechanical silica microcavities, Phys. Rev. A **80**, 021803 (2009).

[69] Q. P. Unterreithmeier, E. M. Weig, and J. P. Kotthaus, Universal transduction scheme for nanomechanical systems based on dielectric forces, Nature **458**, 1001–1004 (2009).

[70] P.-L. Yu, T. P. Purdy, and C. A. Regal, Control of material damping in high-q membrane microresonators, Phys. Rev. Lett. **108**, 083603 (2012).

[71] T. Bagci, A. Simonsen, S. Schmid, L. G. Villanueva, E. Zeuthen, J. Appel, J. M. Taylor, A. Sørensen, K. Usami, A. Schliesser, *et al.*, Optical detection of radio waves through a nanomechanical transducer, Nature **507**, 81–85 (2014).

[72] S. Schmid, T. Bagci, E. Zeuthen, J. M. Taylor, P. K. Herring, M. C. Cassidy, C. M. Marcus, L. G. Villanueva, B. Amato, A. Boisen, *et al.*, Single-layer graphene on silicon nitride micromembrane resonators, J. App. Phys. **115**, 054513 (2014).

[73] O. Arcizet, V. Jacques, A. Siria, P. Poncharal, P. Vincent, and S. Seidelin, A single nitrogen-vacancy defect coupled to a nanomechanical oscillator, Nat. Phys. **7**, 879–883 (2011).

[74] K. Hammerer, M. Aspelmeyer, E. S. Polzik, and P. Zoller, Establishing einstein-poldosky-rosen channels between nanomechanics and atomic ensembles, Phys. Rev. Lett. **102**, 020501 (2009).

[75] A. Jöckel, A. Faber, T. Kampschulte, M. Korppi, M. T. Rakher, and P. Treutlein, Sympathetic cooling of a membrane oscillator in a hybrid mechanical–atomic system, Nature Nano. (2014).

[76] E. Vetsch, D. Reitz, G. Sagué, R. Schmidt, S. T. Dawkins, and A. Rauschenbeutel, Optical interface created by laser-cooled atoms trapped in the evanescent field surrounding an optical nanofiber, Phys. Rev. Lett. **104**, 203603 (2010).

[77] S. Groeblacher, A. Trubarov, N. Prigge, G. D. Cole, M. Aspelmeyer, and J. Eisert, Observation of non-Markovian micromechanical Brownian motion, Nat. Comm. **6** (2015).

[78] M. Metcalfe, Applications of cavity optomechanics, Applied Physics Reviews **1**, 031105 (2014).

[79] A. G. Krause, M. Winger, T. D. Blasius, Q. Lin, and O. Painter, A high-resolution microchip optomechanical accelerometer, Nat. Phot. **6**, 768–772 (2012).